WILEY-VCH

DOI:
Article type: Full Paper

Dual mode strain-temperature sensor with high stimuli discriminability and resolution for smart wearables

Huiyun Xiao[a,b,c], *Shengbin Li*[a,b,c], *Zidong He*[a,b,c], *Yuanzhao Wu*[a,b,c], Zhiyi Gao[a,b,c], *Chao Hu*[b], *Siqi Hu*[b], *Shengding Wang*[a,b,c], *Chao Liu*[b,d], *Jie Shang*[a,b,c], *Meiyong Liao*[e], Denys Makarov[f,*], *Yiwei Liu*[a,b,c,*], *Run-Wei Li*[a,b,c,*]

[a]CAS Key Laboratory of Magnetic Materials and Devices,
Ningbo Institute of Materials Technology and Engineering, Chinese Academy of Sciences, Ningbo 315201, P. R. China

[b]Zhejiang Province Key Laboratory of Magnetic Materials and Application Technology,
Ningbo Institute of Materials Technology and Engineering, Chinese Academy of Sciences, Ningbo 315201, P. R. China

[c]University of Chinese Academy of Sciences, Beijing 100049, P. R. China

[d]School of Material Chemistry, Ningbo University, Ningbo, Zhejiang 315201, P. R. China

[e]National Institute for Materials Science, 1-1 Namiki, Tsukuba, Ibaraki 305-0044, Japan

[f]Helmholtz-Zentrum Dresden-Rossendorf e.V, Institute of Ion Beam Physics and Materials Research, Bautzner Landstrasse 400, 01328 Dresden, Germany

Corresponding author: Yiwei Liu, Denys Makarov, Run-Wei Li

E-mail: liuyw@nimte.ac.cn (Prof. Y. W. Liu); d.makarov@hzdr.de (Dr. D. Makarov); runweili@nimte.ac.cn (Prof. R.-W. Li)

Telephone: +86-574-87617212

Fax: +86-574-87617212

Keyword: Dual-mode sensors, Magnetoelastic effect, Co-based amorphous wire, Thermoelectricity, Smart wearables

Abstract

Strain and temperature are important physiological parameters for health monitoring, providing access to the respiration state, movement of joints and inflammation processes. The challenge for smart wearables is to unambiguously discriminate strain and temperature using a single sensor element assuring a high degree of sensor integration. Here, we report a dual-mode sensor with two electrodes and tubular mechanically heterogeneous structure enabling simultaneous sensing of strain and temperature without cross-talk. The sensor structure consists of a thermocouple coiled around an elastic strain-to-magnetic induction conversion unit, revealing a giant magnetoelastic effect, and accommodating a magnetic amorphous wire. The thermocouple provides access to temperature and its coil structure allows to measure impedance changes caused by the applied strain. The dual-mode sensor also exhibits interference-free temperature sensing performance with high coefficient of 54.49 μV/°C, low strain and temperature detection limits of 0.05% and 0.1 °C, respectively. We demonstrate the use of these sensors in smart textiles to monitor continuously breathing, body movement, body temperature and ambient temperature. The developed multifunctional wearable sensor is needed for applications in early disease prevention, health monitoring and interactive electronics as well as for smart prosthetics and intelligent soft robotics.

1. Introduction

Strain and temperature are important parameters to evaluate physiological conditions. [1-6] Continuous monitoring of respiration (subtle strain variation) and body temperature enables health assessment and early disease diagnosis. Similarly, real-time motion monitoring (larger strain changes) as well as body and ambient temperature during rehabilitation training could protect patients from secondary damage and excessive exercise. [7,8] Therefore, there are strong activities on the realization of elastic dual-mode sensors for strain-temperature detection in the applications of health care, rehabilitation training, human-machine interaction, and soft robots. [9-14] Simultaneous detection of strain and temperature can be realized by either stacking several single-function sensors or arranging them on a flexible substrate. [15-19] However, it is difficult to accommodate the development trend of high integration and miniaturization by planar array, or less accurate to measure with a sensor in the second layer of vertical stack. [20, 21] Developing materials that are both sensitive to strain and temperature changes is an alternative approach. In this respect, sensing materials have been mixed with an elastomer matrix to achieve a single flexible sensor for temperature and strain monitoring, such as carbon nanotubes, [22, 23] ionic liquids, [24] carbon particles, [25] Ag nanowires, [26] graphite, [27] reduced graphene oxide. [28] However, due to the coupled output of the processing signals, this type of sensor has challenges in real-time discrimination of strain and temperature stimuli. [29] We note that also for the sensors, which are stacked or positioned next to each other, the cross-talk is an issue. If there is a temperature change, strain sensor can be affected and vice versa. Therefore, the signal discrimination is a generic problem of multimodal sensorics, which should be solved independent of the technology used for sensor fabrication.

There are two strategies to develop dual-mode sensors that could simultaneously monitor strain and temperature with interference-free output signals. Firstly, stimulus-specific outputs can be obtained by utilizing two physical effects corresponding to strain and temperature stimulation. [30, 31] For instance, Li et al. chose MXene-Ag nanowire-Te nanowire-PEDOT: PSS as a sensitive material to obtain independent sensing outputs of strain and temperature signals by using piezoresistive and thermoelectric effects. [30] Similarly, He et al. fabricated stretchable PEDOT:PSS/CNT/WPU composite films to detect variations of Seeback voltage (thermoelectric effect) and resistance (piezoresistive effect) corresponding to temperature and strain stimuli, respectively. [31] Relying on the structural design to suppress strain or temperature disturbances at a certain sensor area is another potential solution to achieve real-time strain and temperature monitoring without cross-talk. [13, 32-34] To this end, Chhetry et al. decoupled strain and temperature stimuli by designing meander-shaped structures to eliminate the effect of strain on temperature. [13] Chen et al. designed an overall core-shell structure as well as a segmental configuration of thermal and strain-sensitive materials to realize continuous monitoring and separation of strain and temperature. [33] Nevertheless, these sensors are able to transduce and distinguish temperature and strain information using 3 or even more contacts, leading to more cabling during measurement, especially for arrays. [13, 24, 34] Furthermore, for the dual-mode sensors (as shown in **Table 1**), the focus is more on how a single sensor can achieve decoupling of strain and temperature signals, but with compromises on performance such as detection limits and poor strain/temperature resolution performance, which is not sufficient to detecting subtle strain and minor temperature fluctuations. [30-34]

Herein, we report a strain and temperature dual-mode sensor (STDMS) with a tubular mechanically heterogeneous structure and hybrid detection mechanism, enabling real-time sensing of strain and temperature stimuli without cross-talk. Compared with bulk or film sensors, elastic tube-shape sensors are preferred due to their conformal characteristics with fibers enabling their easy assembly in textiles and fulfilling key requirements of wearable electronics including flexibility, breathability, and comfort. [35, 36] Our sensor element consists of a CuNi-Cu (CNC) thermocouple, which is coiled around a strain-to-magnetic induction conversion unit. The latter is based on a heterogeneous structure assembled of a cylindrical PDMS core accommodating Co-based amorphous wires (CoAWs) located between two tube-shaped segments of magnetic composite of NdFeB@PDMS (NP). The coil-shaped thermocouple allows to measure temperature via thermoelectric (TE) effect and is able to output the impedance change corresponding to the strain information. As the thermoelectric voltage corresponding to the measured temperature is not affected by mechanical strain, we can clearly decouple two information channels and avoid cross-talk. Our sensor structure benefits from the giant magnetoelastic (GME) effect of the magnetic composite and high permeability of CoAWs. By tailoring the relative mechanical modulus of the components of the strain-to-magnetic induction conversion unit, we can customize strain sensitivity of the sensor. The STDMS exhibits a high strain sensitivity (gauge factor of 5.29 at larger strain and 1.71 at subtle strain), high temperature coefficient of 54.49 μV/°C, low limit of detection (0.05% strain and 0.1 °C), high response time (strain response of 100-200 ms and temperature response of <1 s), and good cycling stability. We demonstrate performance of STDMS when integrated in textiles to detect physiological signals (such as respiration and body temperature) or monitor motion and ambient temperature simultaneously. Our

sensor technology is relevant for smart wearables (smart textiles and smart skins) in health monitoring and human-machine interaction as well as for smart prosthetics and for the realization of intelligent soft robots. [37-40]

2. Result and Discussion

2.1 Design principle and fabrication process of STDMS

The sensing mechanism and related application of as-designed flexible STDMS are illustrated in **Figure 1a**. To sense strain we design strain-to-magnetic induction conversion unit benefiting from the giant magnetoelastic effect in a NdFeB@PDMS (NP) composite. The magnetization of the composite exhibits a significant change of about 30 mT upon applying 30% strain while stretching the composite (**Figure S1a, b**, Supporting Information), which is comparable to the values reported in the literature. [41, 42] This change in magnetization results in the modification of magnetic induction within the sample, which is captured by simulations (**Figure S2a**, Supporting Information). In particular, the simulation revealed a magnetic field change of 2.8 mT at a distance of 4 mm from the magnetic composite. We note that there is a difference in the distribution of magnetic induction lines even at 0.1% strain, corresponding to a magnetic field variation of about 4 μT (**Figure S2b**, **c**, Supporting Information).

To gain temperature and strain sensitivity within the STDMS element, we prepared a CNC thermocouple with a diameter of about 80 μm (**Figure S3a**, Supporting Information**)** and linear thermoelectric properties (**Figure S3b**, Supporting Information**)**, which is coiled around the strain-to-magnetic induction conversion unit. The thermocouple outputs the voltage induced by the change of temperature relying on the thermoelectric effect. Furthermore, the coil-shaped CNC wire outputs the impedance change corresponding to the actual strain value relying on an LC oscillation circuit (a

circuit in which an inductor (L) and a capacitor (C) are connected in parallel). CoAWs with a diameter of about 120 μm (**Figure S4a**, Supporting Information**)** possessing high magnetic permeability (8000 at f = 1 kHz) and high saturation magnetization (about 0.62 T; **Figure S4a, b**, Supporting Information) are embedded in the strain-to-magnetic induction conversion unit within the solenoid formed by the coiled CNC wire to enhance the change of the measured impedance upon mechanical deformation of the unit. The strain-to-magnetic induction conversion unit containing CoAWs is designed as a mechanically heterogeneous structure, enabling strain sensing capability and mechanical flexibility. Therefore, the developed mechanically heterogeneous structure and distinct physical effects to measure strain and temperature enable realization of STDMS.

Figure 1b demonstrates schematics of the fabrication of STDMS. The strain-to-magnetic induction conversion unit consists of two magnetic composites shaped as tubular structures located at both ends of the STDMS. The tube-shaped composites (inner diameter of 1 mm; outer diameter of 1.6 mm) were fabricated by mixing NdFeB particles with PDMS and curing them in a mold with a cylindrical core (**Figure 1c**). Subsequently, the middle region of the mold is filled with pure PDMS and cured to realize a cylinder-shaped PDMS object (diameter: 1 mm). Then the magnetic composite is magnetized with impulse field of 50 kOe that reorients NdFeB micromagnets in the soft polymer matrix. By adjusting the direction of the axial (cyan arrow) and magnetized impulse fields (blue arrow), we can realize tube-shaped magnetic composites with different magnetic sensitivity directions (**Figure 1d, Figure 1g**). The magnetic stray field of the composites, determined using a magnetic field visualizing indicator films, exhibits a significant anisotropy in the axial and longitudinal directions due to the different orientations of the micromagnets (**Figure 1e, f, h, i**).

The final step of the STDMS fabrication is the assembly of the CoAW in the middle region of the PDMS cylinder and winding the CNC thermocouple coil for impedance signal output and temperature detection. The prepared hybrid elastic tube with mechanocombinatorially segmented structure exhibits high elongation at break of 124% (**Figure S5,** Supporting Information**)** and excellent stretching (**Figure 1j**), bending (**Figure 1k**) and twisting (**Figure 1l**) performance, and maintains good flexibility (elongation at break > 50%) after assembling CoAW and winding coils (**Figure 1m** and **Figure S5,** Supporting Information).

2.2 Investigation of the factors that affect the strain sensing performance

The strain sensing mechanism of the STDMS is based on the measurement of electric inductance of the winding coils upon deformation of the magnetic composite. Deformations lead to the change of the magnetic field in the interior of the coil, which is enhanced due to the high permeability of the CoAW. The latter offers up to 300% changes in magnetic permeability with increasing magnetic field (**Figure S6,** Supporting Information**)**. Inductance of a solenoid, L, with a magnetic core is described as follows, [43]

$$L = \mu \times A_e \times N^2 / l_m \quad (1)$$

where μ is the permeability of the magnetic core (i.e., CoAW), A_e is the cross-sectional area of the solenoid, N is the number of turns of the coil, and l_m is the length of magnetic core. Combining the solenoid with inductance L with a capacitor with capacitance C (provided by the impedance analyzer), the impedance Z of the electric circuit at angular frequency ω can be written as, [44]

$$Z = R + i(\omega L - 1/(\omega C)) \quad (2)$$

where R is the circuit resistance. As L contains information on the applied strain, the measurement of the complex impedance provides access to the strain in the STDMS. The relative change of the impedance with strain represented in percents is defined as η:

$$\eta = \frac{\Delta Z}{Z_0}(\%) = (\frac{Z}{Z_0} - 1) \times 100\% \quad (3)$$

where Z and Z_0 are impedance values with and without applied external strain, respectively. According to the Equation (1-3), there are numerous parameters, which lead to the change of the sensor impedance. Those parameters include the distance between tubular-shaped magnetic composites and CoAWs (defined as α), the length of the tubular-shaped magnetic composites (β), the length of nonmagnetic cylinder (δ), the magnetic powder content in the magnetic composite (λ), the magnetization direction of the tubular-shaped magnetic composites (θ), the number of turns of the CNC coil (N) and the measurement frequency (f). The relevant geometrical parameters are indicated in insert figure of **Figure 2a**. The purpose of regulating all parameters is to make the magnetic field provided by the magnetic composite match the magnetic sensitivity interval corresponding to the maximum impedance variation of the CoAW (**Figure 2a**).

First, we observe that if the value of α increases from 0 mm to 6 mm, η reaches maximum of 23.5% at α = 4 and for the applied strain of 30% (**Figure S7,** Supporting Information**)**. The changes in the parameter β have minor effect on the impedance of the STDMS (**Figure S8,** Supporting Information). The different influence of α and β on η can be explained by their varying influence on the variation of the magnetic field during the stretching process. The finite element analysis (FEA) data (**Figure S9**, Supporting Information**)** indicates significant magnetic field variation (>900%) for the case when α increases from 0 mm to 4 mm**,** leading to greater η. Moreover, the changes in δ could also affect the distribution of the magnetic field in the region of CoAWs, which in turn affects

η (**Figure S10,** Supporting Information). The value of η is maximized for δ = 22 mm. The observed dependence of η on δ could be attributed to a narrow range of magnetic fields for which the used CoAW is not saturated.

The parameter λ has a significant effect on the magnetic field magnitude. The magnetization of the composite increases with the content of magnetic powder (**Figure S11**, Supporting Information). We observe that η is largest at λ = 1:2, which is used in the following experiments (**Figure S12**, Supporting Information). It is reported that addition of microparticles affects mechanical properties of the elastic matrix (increase in modulus and a decrease in elongation at break). [45] The typical tensile stress–strain curves of the fabricated magnetic composites with different λ are presented in **Figure S13a** (Supporting Information). Compared with the tube-shaped PDMS structure without magnetic loading, magnetic composites reveal increased tensile strength and slightly decreased fracture elongation strain. Still, the mechanical properties of the composites meet morphological requirements for wearable e-skins. Furthermore, the magnetic composites with hollow structure show a modulus of 0.547 MPa, which is lower than solid structure with modulus of 1.7 MPa, facilitating the subsequent regulation of the relative modulus magnitude to the nonmagnetic cylinder (**Figure S13b**, Supporting Information). In addition, a large η with a maximum value of 23.7% is achieved at strain of 30% when the pulsing magnetic field is oriented along the axis of tube-shaped composite (i.e., θ = 0°, **Figure S14**, Supporting Information) resulting in the axial distribution of magnetic induction lines along the composite.

To monitor the impact of these parameters, it is instructive to introduce the sensitivity factor ρ, which is defined as follows:

$$\rho = (\eta_{max}-\eta_{min})/(\varepsilon_{max}-\varepsilon_{min}) \quad (4)$$

where η_{max} and η_{min} are the values of the normalized impedance change ($\Delta Z/Z_0$) at maximum and minimum strain, respectively, ε_{max} and ε_{min} is the maximum and minimum strain. The value of ρ reaches maximum of 77.19% at α = 4 mm, δ = 22 mm, λ = 1:2, and θ = 0° (**Figure 2b**), which are selected as the optimal parameters for the following experiments. Meanwhile, η is also affected by the number of turns of the CNC coil and the measurement frequency. Although the coil with 400 turns reveals the largest η (**Figure 2c**), it results in the increase of the sensor size. Hence, for further experiments we selected the device accommodating a coil with 300 turns. Furthermore, we observe that η reaches the maximum value at 500 kHz (**Figure 2d** and **Figure S15**, Supporting Information). In summary, we obtain STDMS architectures with optimal parameter, including α = 4 mm, β=22 mm, λ=1:2, θ=0°, N=300 turns, respectively, which were also used as the parameters for the subsequent measurements.

2.3 Electromechanical characterization of the STDMS

A customized sensitivity facilitates the realization of personalized stretchable electronics for monitoring strain with different amplitudes. [46] We explore mechanocombinatorial approach to adjust sensitivity of strain sensors relying on the mechanically heterogeneous structure **(Figure 3a)**. The Young's modulus of the magnetic composites and the nonmagnetic cylinder are defined as E_1 and E_2, respectively. Strain redistribution across the STDMS can be achieved by adjusting the relative magnitudes of E_1 and E_2, which has been confirmed by finite element analysis simulations.

The Young's modulus can be tailored by changing the mass ratio of base monomer to curing agent. [47] After straightforward but tedious optimization of the ratio of base monomer to curing agent, we fabricated the STDMS with $E_1 < E_2$ (referred to as STDMS-

E_2). This structure is based on the magnetically loaded PDMS with the mass ratio of base monomer to curing agent of 20:1 and pure PDMS tube with the ratio of 10:1. For this structure, E_1 = 0.166 MPa and E_2 = 0.392 MPa (**Figure S16a**, Supporting Information). Similar optimization allowed us to prepare the STDMS with $E_1 > E_2$ (referred to as STDMS-E_1) using magnetically loaded PDMS with the ratio of 14:1 and pure PDMS tube with the ratio of 18:1. This structure is characterised by E_1 = 0.576 MPa and E_2 = 0.239 MPa (**Figure S16b**, Supporting Information).

To enable detection of subtle strains, the STDMS-E_1 is a preferred option. Indeed, this STDMS relies on the structure change of the nonmagnetic cylinder. In this case, based on the data discussed in section 2.2, an increase of α is beneficial to provide a larger variation of the magnetic field resulting in a stronger sensor response.

In the case of STDMS-E_2, at initial elongation stages, the primarily deformation concerns the magnetic composites of strain-to-magnetic induction conversion unit (change of the β parameter), which does not affect the sensor response. Only at a substantial level of strain, the nonmagnetic cylinder starts elongating leading to the change of the α parameter resulting in the sensor response.

The variation of η values with increasing strain for the STDMS with $E_1 : E_2 = 2 : 5$ and $E_1 : E_2 = 5 : 2$ are shown in **Figure 3b**. The ratio of the relative change of the η value is defined as:

$$GF = \Delta\eta/\Delta\varepsilon \quad (5)$$

Where Δη is the relative rate of change of impedance variation and $\Delta\varepsilon$ is the change of the applied strain. Here, this equation is different from Equation (4), where the former represents the instantaneous rate of change of impedance with strain, while the latter represents the average rate of change of impedance with strain. For instance, while at

small strain values the STDMS-E_2 structure is characterized by GF of 0.61, the STDMS-E_1 exhibits GF of 1.71. On the contrary, when the strain increases to about 20%, the STDMS-E_2 structure performs better revealing GF of 5.29, which is substantially higher than GF of STDMS-E_1 of 0.93.

The detection limit of the strain sensor is studied in **Figure 3c**. The STDMS-E_1 structure allows to detect strains down to 0.05% with a resolution of 0.1% (corresponds to the change of the sensor impedance of 0.14%). This high resolution is superior to most strain-temperature dual-mode sensors as previous literature reports (**Table 1**). **Figure 3d** demonstrates a steep increase of η values for the STDMS-E_2 at larger strains. The response time at a rapid loading and unloading process is another relevant parameter in the application of stretchable strain sensors. As shown in **Figure 3e**, the STDMS exhibits a rapid response time of 0.18 s and a relaxation time of 0.16 s, which is comparable to most strain-temperature dual-mode sensors. Furthermore, the STDMS exhibits good stability over 1000 stretching and releasing cycles between 0 and 15% strain as shown in **Figure 3f**.

2.4 Temperature sensing performance of the STDMS

Figure 4 shows the temperature sensing performance of the STDMS. The instantaneous output voltage variation as a function of the temperature changes of 0 - 55 ^{o}C at a rate of 5 ^{o}C during the heating and cooling process is summarized in **Figure 4a**. Due to the Seeback effect in the CNC thermocouple, we observe a close to linear increase in the voltage output with increasing temperature and reach a maximum output voltage of 2.997 mV at a temperature change of 55 °C. The temperature response of the thermoelectric sensor is quantified as:

$$\Delta V = V_1 - V_0 = S_T \times (T_1 - T_0) \quad (6)$$

where S_T denotes the Seebeck coefficient, V_1 and V_0 are voltage outputs at temperatures T_1 and T_0, respectively. The S_T of the CNC thermocouple is calculated to be 54.49 μV/°C, which can be further enhanced by joining several thermocouples in series (**Figure S17a**, Supporting Information). A single CNC thermocouple incorporated within the STDMS structure reveals sensitivity comparable to common thermoelectric materials (**Figure S17b**, Supporting Information). Accordingly, The STDMS exhibit accurate detection of temperature gradient within 0.1 °C with an output voltage of ~5 μV (**Figure 4b**).

Then we set the target temperature within the physiologically relevant temperature range (35 - 45 °C) and study the variation of the output voltage over ten heating and cooling cycles (**Figure 4c**), indicating an excellent temperature stability and repeatability. Temperature response time is another important parameter for temperature sensors. The STDMS shows a rapid response time of 0.9 (0.3) s when the sensor is approached with a heating (cooling) source of 50 (10) °C (**Figure 4d**), which could be attributed to high thermal conductivity of metal wire.

2.5 Independent perception and distinction of strain and temperature stimuli

To validate that the STDMS could realize independent detection and distinction of strain and temperature stimuli, we perform characterization as depicted in **Figure 5**. The strain and temperature stimuli were simultaneously applied to the sensor and the mutual effect of both stimuli was measured (**Figure 5a)**. **Figure 5b** displays changes of the impedance of the STDMS with applied strain from 0 to 30% at 25, 45, 65 °C. The curves measured at different temperatures almost coincide with each other. Furthermore, the

factor κ is defined as Equation (7) to describe the degree to which the impedance change is affected by temperature.

$$\kappa = ((\Delta Z/Z)@_{Tx}/(\Delta Z/Z)@_{T0}\text{-}1) \times 100\% \quad (7)$$

where $(\Delta Z/Z)@_{Tx}$ and $(\Delta Z/Z)@_{T0}$ denote impedance change rate at temperature T_x (45 ºC, 65 ºC) and T_0 (25 ºC) respectively. It is observed that the variation of the factor k is always less than 3% as the temperature increases to 65 °C (**Figure 5c**). As a result, the strain sensing ability of the STDMS is almost unaffected by temperature. In fact, in the STDMS with tubular heterostructure, strain is detected through the impedance of the solenoid with CoAWs in reaction to the variation of the magnetic field. The effect of temperature on the magnetic field provided by strain-to-magnetic induction conversion unit and the magnetic properties (especially permeability) of CoAWs determines its interference with strain perception capability. As shown in **Figure S18a-c** (Supporting Information), the remanent magnetization of the magnetic composites remains stable (relative changes < 5%) with increasing temperature under stretched and unstretched states. Meanwhile, the permeability of CoAWs remains the same with the temperature decreasing from 100 ℃ (well below the Curie temperature of CoAWs) to room temperature (**Figure S19**, Supporting Information**)**. Therefore, there is negligible effect of temperature on the strain sensing performance.

Similarly, the impact of mechanical strain on the temperature sensing performance of the sensor were carried out (**Figure 5d**). Indeed, as the thermocouple measures voltage only, any changes in the electrical resistance of the wires do not affect the thermoelectric effect. Furthermore, according to finite element simulations of the strain distribution during the stretching process (**Figure 3a**), there is no distribution of strain in the region where the CNC thermocouple is mounted. As indicated by the model and experimental

results, the output voltage of the STDMS shows a linear increase with the temperature gradient from 0 to 55 °C, the output voltage curves almost coincide at applied strains of 0, 10%, 20% and 30%. Meanwhile, the factor κ is defined as Equation (8) to describe the degree to which the impedance change is affected by temperature.

$$\psi = ((\Delta V)@\varepsilon_x/(\Delta V)@\varepsilon_0\text{-}1) \times 100\% \quad (8)$$

where $(\Delta V)@\varepsilon_x$ and $(\Delta V)@\varepsilon_0$ denote voltage variation rate at strain ε_x (0.1, 0.2, 0.3) and ε_0 (0) respectively. We can find that the ψ remains stable as strain increases to 30%, indicating a negligible effect of strain on the temperature sensing performance (**Figure 5e**). Meanwhile, according to Faraday effect, the changing magnetic flux could also generate a voltage in the coil. The output Faraday voltage of STDMS was measured for 10 cycles at a stretching rate of 300 mm/min and shown in Figure S20 (Supporting Information). there is no significant and regular output voltage, indicating that the changing magnetic flux could not affect the voltage output.

As we known, developed functional nanomaterials or hybrid micro/nanostructures based on different transduction mechanisms is effective strategy to sense multiple stimulation, and then converting external stimuli into electrical signals with corresponding output electrodes. [13, 24, 34] These transduction methods generally include piezoresistivity, capacitance, and piezoelectricity, etc. For the dual model sensor based on a single transduction mechanism, such as piezoresistivity (i.e., transducing force/temperature variations into resistance change), more electrodes are required to output signals and achieve signal discrimination. Dependent on two different transduction mechanisms in a single sensor could achieve the distinction of different stimuli. But when the mechanisms contain capacitive transduction mechanism, more than 3 electrodes are needed to output the signal. Together with strain and temperature sensing performance,

the STDMS with only two contacts exhibits superior detection limits for both strain and temperature compared to other strain-temperature dual-mode sensors, as well as perfect strain and temperature stimulus discriminability (**Figure 5f, Table 1**, **Figure S21**, Supporting Information).

2.6 Dual-mode applications of the STDMS

Tube-shaped sensors of the present work could be easily integrated in a textile at joints or chest cavity and used for physiological signal detection of the human body or temperature detection of the environment (**Figure 6a**). Various single stimulus signals could be monitored by the STDMS in real time and visualized by a display device, including subtle strains, such as normal breathing or deep breathing (**Figure 6b**, **Video S1**, Supporting Information), and swallow (**Figure 6c**, **Video S2**, Supporting Information). Furthermore, the sensor detects larger strains at body joints, such as knee flexion during walking and running (**Figure 6d)**, finger (**Figure S22a**, Supporting Information**)**, wrist (**Figure S22b**, Supporting Information**)**, elbow (**Figure S22c**, Supporting Information**)**, neck (**Figure S22d**, Supporting Information**)** bending. In addition, a temperature rises of approximately 1 °C during a ten minute running exercise can be measured (**Figure 6e**).

To demonstrate the capability of the STDMS to independently and continuously sense strain and temperature, we mounted the STDMS on a breathing belt (**Figure S23**, Supporting Information**)** and glove (**Figure S24**, Supporting Information**)** with cotton yarn. We eliminate the effect of AC current applied during the impedance measurement on the thermocouple voltage output signal by adjusting the controlling software (**Figure S25**, Supporting Information**)** and hardware (**Figure 6f, Figure S26**, Supporting

Information). In this way, we realize temporary isolation of the LCR meter when reading voltage signals by the voltmeter.

It is known that the body temperature is relatively constant without strenuous exercise (**Figure S27**, Supporting Information**)**. Hence, the sensor can not only detect the variation of the body temperature during exercise, but also realize monitoring of ambient temperature under stationary conditions (**Video S3**, Supporting Information). In this case, the human body acts as the reference side of the thermocouple. **Figure 6g** illustrates the real-time and continuous monitoring of respiration and ambient temperature by the STDMS mounted on a breathing belt. Generally, the ambient temperature is below body temperature. As the environment temperature rises by about 4°C (from 25 °C to 29 °C), the temperature gradient decreases and the output voltage decreases accordingly. the voltage measured by the thermocouple monotonically decays by ~150 μV corresponding to temperature variation of 3 °C. Meanwhile, the impedance rises and falls repeatedly between 191.4 and 192.6 Ω with the exhalation and inhalation. In addition, The STDMS mounted to a glove could be applied to identify water temperature and the motion of grasping the water cup (**Figure S28**, Supporting Information**)**.

3. Conclusions

In summary, we demonstrate a dual-mode elastic sensor consisting of a tubular mechanically heterogeneous structure and featuring a hybrid detection mechanism. The sensor enables real-time measurement of strain and temperature stimuli without interference. Our sensing element consists of three parts: (i) a strain-to-magnetic induction conversion unit revealing giant magnetoelastic effect, (ii) amorphous Co-based wire with high permeability and (iii) a thermocouple wound around the sensing structure

and providing access to the information on temperature as well as enabling measurement of the impedance change corresponding to the mechanical strain. The sensing element can detect low and large strain values by tailoring mechanical modulus of the components of the strain-to-magnetic induction conversion unit. The gauge factors obtained for our sensing elements are 5.29 at larger strain and 1.71 at subtle strain. Relying on the thermoelectric voltage measured using the on-board thermocouple, our STDMS exhibits interference-free temperature sensing performance with high coefficient of 54.49 μV/°C. Furthermore, our dual-mode elastic sensor can detect strain as low as 0.05% with the resolution of 0.1% and temperature with the accuracy of 0.1 °C. The sensor has excellent mechanical stability and does not reveal any degradation of performance upon repetitive mechanical deformation for 1000 stretching and releasing cycles. To highlight it application potential, we integrated the developed STDMS in textile to detect breathing/human-movement and body temperature continuously and independently, as well as ambient temperature. The proposed sensing platform is relevant for multifunctional wearable electronics for applications in early disease prevention, health monitoring, and human-machine interaction. Furthermore, we envision broad applicability of the STDMS for prosthetics and also for robotic applications including realization of intelligent soft robot systems. [37, 39, 48]

4. Experimental Section

4.1 Fabrication of the STDMS

STDMS are prepared in a two-step curing process. Firstly, PDMS (including pre-polymer and its curing agent; Sylgard 184, Dow Corning, USA) and NdFeB powder (particle size ~5 μm, XND Co. PRC) with a mass ratio of 2:1 was mixed by mechanical stirring and injected into both ends of a mold with a cylindrical core of 1 mm diameter.

After removing air bubbles by a vacuum extraction device, the so-formed magnetically loaded elastic tube (i.e., magnetic composites) was cured in a vacuum oven at 60 °C for 4 h. Pure PDMS is then poured into the middle area of the mold to form nonmagnetic cylinder and connect the two tube-shaped magnetic composites. In this case, we formed strain-to-magnetic induction conversion unit (inner and outer diameter of 1 mm and 1.6 mm, respectively) with mechanically heterogeneous structure consisting of magnetic composites and nonmagnetic cylinder. By changing the mass ratio of basic monomer and curing agent of PDMS in magnetic composites and non-magnetic cylinders, we fabricated the strain-to-magnetic induction conversion unit with $E_1 < E_2$ and $E_1 > E_2$. As for STDMS-E_2 with $E_1 : E_2 = 2 : 5$, the structure is based on the magnetically loaded PDMS with the mass ratio of base monomer to curing agent of 20:1 and pure PDMS tube with the ratio of 10:1. Similarly, the STDMS-E_1 ($E_1 : E_2 = 5 : 2$) using magnetically loaded PDMS with the ratio of 14:1 and pure PDMS tube with the ratio of 18:1.

The strain-to-magnetic induction conversion unit is magnetized in a pulsed magnetic field of 50 kOe using magnaflux generator (MMPM10, UK). Afterwards, high-modulus (65.47 MPa, (**Figure S29,** Supporting Information) PVC (polyvinyl chloride) plastic tubes (inner and outer diameters of 0.6 mm and 1 mm, respectively) containing CoAWs (diameter of 140 μm, composition of the alloy is $Co_{69}Fe_4(B,C)_{16}Si_7Cr_4$, **Figure S30,** Supporting Information, fabricated using rapid melt quenching method [49]) were inserted into a nonmagnetic cylinder. Here, the high-modulus PVC can prevent CoAWs from being interfered by stress that affects the impedance change. The length of the CoAWs is slightly shorter (4 mm) than the nonmagnetic cylinder to provide optimal magnetic field variation.

The CNC thermocouple consists of two wires (Cu and CuNi; each 80 μm diameter), and the two wires are soldered at one end. Both wires of the thermocouple are wound around the region of CoAWs by using a winding machine. In this way, we prepare a tight inductance coil with tunable number of windings (100-500 turns).

4.2 Microscopy characterization

Scanning electron microscope (SEM) imaging of strain-to-magnetic induction conversion unit was obtained by a microscope (Sirion200, FEI, USA). Photographs of the STDMS were taken by a digital camera.

4.3 Strain measurement of the STDMS

Strain measurement of the STDMS was performed via utilizing a computer controlled material testing machine (Instron 5943, USA) at the rate of 10 mm/min. Repetitive loading and unloading testing is performed by using a laboratory tensile test machine. Impedance of CoAWs was measured using an impedance analyzer (Hioki IM3570). The LC oscillation circuit is composed of a CNC thermocouple inductor coil and a capacitor provided by the impedance analyzer. The output impedance data reading is controlled by a program written in LabVIEW (National Instruments, USA).

4.4 Temperature measurement of the STDMS

The CNC thermocouple for the detection of temperature was obtained by soldering one end of CuNi wire and Cu wire using tin. During the measurement, we keep the temperature at the reference side (i.e., the non-soldered side) of the thermocouple stable by a holding device, and use a high precision commercial thermometer to monitor temperature changes at the reference side. The soldered part of the thermocouple is coiled around the magnetic cylinder as measurement side to detect human body temperature. To measure ambient temperature, we preset the desired temperature in a lab using a

commercial air conditioning system. The output voltage generated by the temperature gradient is measured by a voltmeter (Keithley 34420A, Keithley Instruments, USA), and the output voltage data reading is controlled by a program written in LabVIEW (National Instruments, USA).

4.5 Magnetic properties characterization

The magnetic field for testing impedance of individual CoAWs is provided by a Helmholtz coil setup. The magnetic field is measured by a Gauss meter (AFG 3101C, Tektronix, USA). The required current is provided by a current source device (Keithley 237, Keithley Instruments, USA). The hysteresis analysis of the strain-to-magnetic induction conversion unit is analyzed by the Magnetic Property Measurement System (MPMS, SQUID-VSM, USA) at room temperature. The distribution of magnetic induction line of the magnetic composites was determined by a magnetic field visualizing indicator films (NIANCI Technology Co., PRC). The permeability analysis of Co-based amorphous cores wound by ribbons at different temperatures was performed by an impedance analyzer (Agilent 4294 A, USA).

Supporting Information

Supporting Information is available from the Wiley Online Library or from the author.

Acknowledgments

This work was supported by the National Natural Science Foundation of China (51931011, 51971233, 52127803, 61774161, 62174165, M-0152, U20A6001 and U1909215), the External Cooperation Program of Chinese Academy of Sciences (174433KYSB20190038, 174433KYSB20200013), the Instrument Developing Project

of the Chinese Academy of Sciences (YJKYYQ20200030), K.C. Wong Education Foundation (GJTD-2020-11), Chinese Academy of Sciences Youth Innovation Promotion Association (2018334), CAS President's International Fellowship Initiative (PIFI) (2019PE0019), Zhejiang Provincial Key R&D Program(2021C01183), Public Welfare Technical Applied Research Project of Zhejiang Province (LGG19F010006), Ningbo Scientific and Technological Innovation 2025 Major Project (2019B10127, 2020Z022). German Research Foundation (DFG) grants MA 5144/13-1, MA 5144/28-1 and Helmholtz Association of German Research Centres in the frame of the Helmholtz Innovation Lab "FlexiSens".

Received: ((will be filled in by the editorial staff))
Revised: ((will be filled in by the editorial staff))
Published online: ((will be filled in by the editorial staff))

Reference

[1] J. C. Yang, J. Mun, S. Y. Kwon, S. Park, Z. Bao, S. Park, *Adv. Mater.* **2019**, 31, e1904765.

[2] T. Someya, M. Amagai, *Nat. biotechnol.* **2019**, 37, 382.

[3] X. Chen, R. Z. Li, G. Y. Niu, M. Y. Xin, G. Z. Xu, H. Y. Cheng, L. Yang, *Chem. Eng. J.* **2022**, 444, 136631.

[4] Y. Ma, Y. Zhang, S. Cai, Z. Han, X. Liu, F. Wang, Y. Cao, Z. Wang, H. Li, Y. Chen, X. Feng, *Adv. Mater.* **2020**, 32, e1902062.

[5] G. Chen, X. Xiao, X. Zhao, T. Tat, M. Bick, J. Chen, *Chem. Rev.* **2022**, 122, 3259.

[6] K.K. Zhai, H. Wang, Q.L. Ding, Z.X. Wu, M.H. Ding, K. Tao, B.-R. Yang, X. Xie, C.W. Li, J. Wu, *Adv. Sci.* **2022**, 2205632.

[7] J. W. Chen, Y. T. Zhu, X. H. Chang, D. Pan, G. Song, Z. H. Guo, N. Naik, *Adv. Funct. Mater.* **2021**, 31, 2104686.

[8] Y. Wang, C. Xu, X. Yu, H. Zhang, M. Han, *Mater. Today Phys.* **2022**, 23, 100647.

[9] K. Xu, Y. Lu, K. Takei, *Adv. Mater. Technol.* **2019**, 4, 1800628.

[10] M. Ilami, H. Bagheri, R. Ahmed, E. O. Skowronek, H. Marvi, *Adv. Mater.* **2021**, 33, e2003139.

[11] G. Ge, Y. Lu, X. Qu, W. Zhao, Y. Ren, W. Wang, Q. Wang, W. Huang, X. Dong, *ACS nano* **2020**, 14, 218.

[12] Y. Pang, X. Xu, S. Chen, Y. Fang, X. Shi, Y. Deng, Z.-L. Wang, C. Cao, *Nano Energy* **2022**, 96, 107137.

[13] A. Chhetry, S. Sharma, S. C. Barman, H. Yoon, S. Ko, C. Park, S. Yoon, H. Kim, J. Y. Park, *Adv. Funct. Mater.* **2020**, 31, 2007661.

[14] S.H. Lin, L.T. Cao, Z.C. Lv, J. Ren, S.J. Ling, *Adv. Fiber Mater.* **2022**, 4, 214.

[15] A. Ahmed, Y. S. Guan, I. Hassan, C. Ling, Z. Li, I. Mosa, G. Phadke, P. R. Selvaganapathy, S. Q. Chang, S. Q. Ren, *Nano Energy* **2020**, 75, 105044.

[16] Q. Hua, J. Sun, H. Liu, R. Bao, R. Yu, J. Zhai, C. Pan, Z. L. Wang, *Nat. commun.* **2018**, 9, 244.

[17] T. Q. Trung, S. Ramasundaram, B. U. Hwang, N. E. Lee, *Adv. Mater.* **2016**, 28, 502.

[18] S. Harada, W. Honda, T. Arie, S. Akita, K. Takei, *ACS nano* **2014**, 8, 3921.

[19] M. Saeidi-Javash, Y. Du, M. Zeng, B. C. Wyatt, B. Zhang, N. Kempf, B. Anasori, Y. Zhang, *ACS Appl. Electron. Mater.* **2021**, 3, 2341.

[20] H. Song, G. Luo, Z. Ji, R. Bo, Z. Xue, D. Yan, F. Zhang, K. Bai, J. Liu, X. Cheng,

W. Pang, Z. Shen, Y. Zhang, *Sci. Adv.* **2022**, 8, eabm3785.

[21] K. Myny, *Nat. Electron.* **2018**, 1, 30.

[22] Y. Li, C. Zheng, S. Liu, L. Huang, T. Fang, J. X. Li, F. Xu, F. Li, *ACS Appl. Mater. Interfaces* **2020**, 12, 23764.

[23] N. Jiang, H. Li, D. W. Hu, Y. Q. Xu, Y. X. Hu, Y. T. Zhu, X. Y. Han, G. Y. Zhao, J. W. Chen, X. H. Chang, M. Xi, Q. Yuan, *Compos. Commun.* **2021**, 27, 100845.

[24] S. T. Yang, C. W. Li, N. X. Wen, S. H. Xu, H. Huang, T. Z. Cong, Y. P. Zhao, Z. Fan, K. Liu, L. J. Pan, *J. Mater. Chem. C* **2021**, 9, 13789.

[25] M. Lin, Z. Zheng, L. Yang, M. Luo, L. Fu, B. Lin, C. Xu, *Adv. Mater.* **2022**, 34, e2107309.

[26] R. Yin, S. Y. Yang, Q. M. Li, S. D. Zhang, H. Liu, J. Han, C. T. Liu, C. Y. Shen, *Sci. Bull.* **2020**, 65, 899.

[27] L. J. Lu, B. Yang, J. Q. Liu, *Chem. Eng. J.* **2020**, 400, 125928.

[28] L. Z. Chen, M. C. Weng, P. D. Zhou, F. Huang, C. H. Liu, S. S. Fan, W. Zhang, *Adv. Func. Mater.* **2019**, 29, 1806057.

[29] J. Gu, J. Huang, G. Chen, L. Hou, J. Zhang, X. Zhang, X. Yang, L. Guan, X. Jiang, H. Liu, *ACS Appl. Mater. Interfaces* **2020**, 12, 40815.

[30] F. Li, Y. Liu, X. Shi, H. Li, C. Wang, Q. Zhang, R. Ma, J. Liang, *Nano Lett.* **2020**, 20, 6176.

[31] X. He, Y. Hao, M. He, X. Qin, L. Wang, J. Yu, *ACS Appl. Mater. Interfaces* **2021**, 13, 60498.

[32] S. P. Zhang, A. Chhetry, M. Abu Zahed, S. Sharma, C. Park, S. Yoon, J. Y. Park, *Npj Flex. Electron.* **2022**, 6, 11.

[33] J. Chen, H. Wen, G. Zhang, F. Lei, Q. Feng, Y. Liu, X. Cao, H. Dong, *ACS Appl.*

Mater. Interfaces **2020**, 12, 7565.

[34] Y. Xie, R. Xie, H. C. Yang, Z. Chen, J. Hou, C. R. Lopez-Barron, N. J. Wagner, K. Z. Gao, *ACS Appl. Mater. Interfaces* **2018**, 10, 32435.

[35] Y. He, Q. Gui, Y. Wang, Z. Wang, S. Liao, Y. Wang, *Small* **2018**, 14, e1800394.

[36] R. Wu, L. Ma, C. Hou, Z. Meng, W. Guo, W. Yu, R. Yu, F. Hu, X. Y. Liu, *Small* **2019**, 15, e1901558.

[37] M. Ha, G. S. Canon Bermudez, J. A. Liu, E. S. Oliveros Mata, B. A. Evans, J. B. Tracy, D. Makarov, *Adv. Mater.* **2021**, 33, e2008751.

[38] Y. Wu, Y. Liu, Y. Zhou, Q. Man, C. Hu, W. Asghar, F. Li, Z. Yu, J. Shang, G. Liu, M. Liao, R. W. Li, *Sci. robot.* **2018**, 3, eaat0429.

[39] F. Khoshmanesh, P. Thurgood, E. Pirogova, S. Nahavandi, S. Baratchi, *Biosens. Bioelectron*. **2021**, 176, 112946.

[40] Q.L. Ding, H. Wang, Z.J. Zhou, Z.X. Wu, K.Tao, X.C. Gui, C. Liu, W.X. Shi, J. Wu, *SmartMat.* **2023**, 4, e1147.

[41] Y. Zhou, X. Zhao, J. Xu, Y. Fang, G. Chen, Y. Song, S. Li, J. Chen, *Nat. mater.* **2021**, 20, 1670.

[42] X. Zhao, G. Chen, Y. Zhou, A. Nashalian, J. Xu, T. Tat, Y. Song, A. Libanori, S. Xu, S. Li, J. Chen, *ACS nano* **2022**, 16, 6013.

[43] R. Wu, L. Ma, S. Liu, A. B. Patil, C. Hou, Y. Zhang, W. Zhang, R. Yu, W. Yu, W. Guo, X. Y. Liu, *Mater. Today Phys.* **2020**, 15, 100243.

[44] M. H. Phan, H. X. Peng, *Prog. Mater. Sci.* **2008**, 53, 323.

[45] J. Gao, L. Wang, Z. Guo, B. Li, H. Wang, J. Luo, X. Huang, H. Xue, *Chem. Eng. J.* **2020**, 381, 122778.

[46] S. Pan, Z. Liu, M. Wang, Y. Jiang, Y. Luo, C. Wan, D. Qi, C. Wang, X. Ge, X. Chen,

Adv. Mater. **2019**, 31, e1903130.

[47] A. A. Bhagat, P. Jothimuthu, I. Papautsky, *Lab Chip* **2007**, 7, 1192.

[48] S. L. T. Kim, T. Hong, G. Shin, T. Kim, Y. Park, *Sci. robot.* **2020**, 5, eabc6878.

[49] D. Estévez, A. He, C. Chang, Q. Man, X. Wang, R.-W. Li, *J. Magn. Magn. Mater.* **2015**, 393, 278.

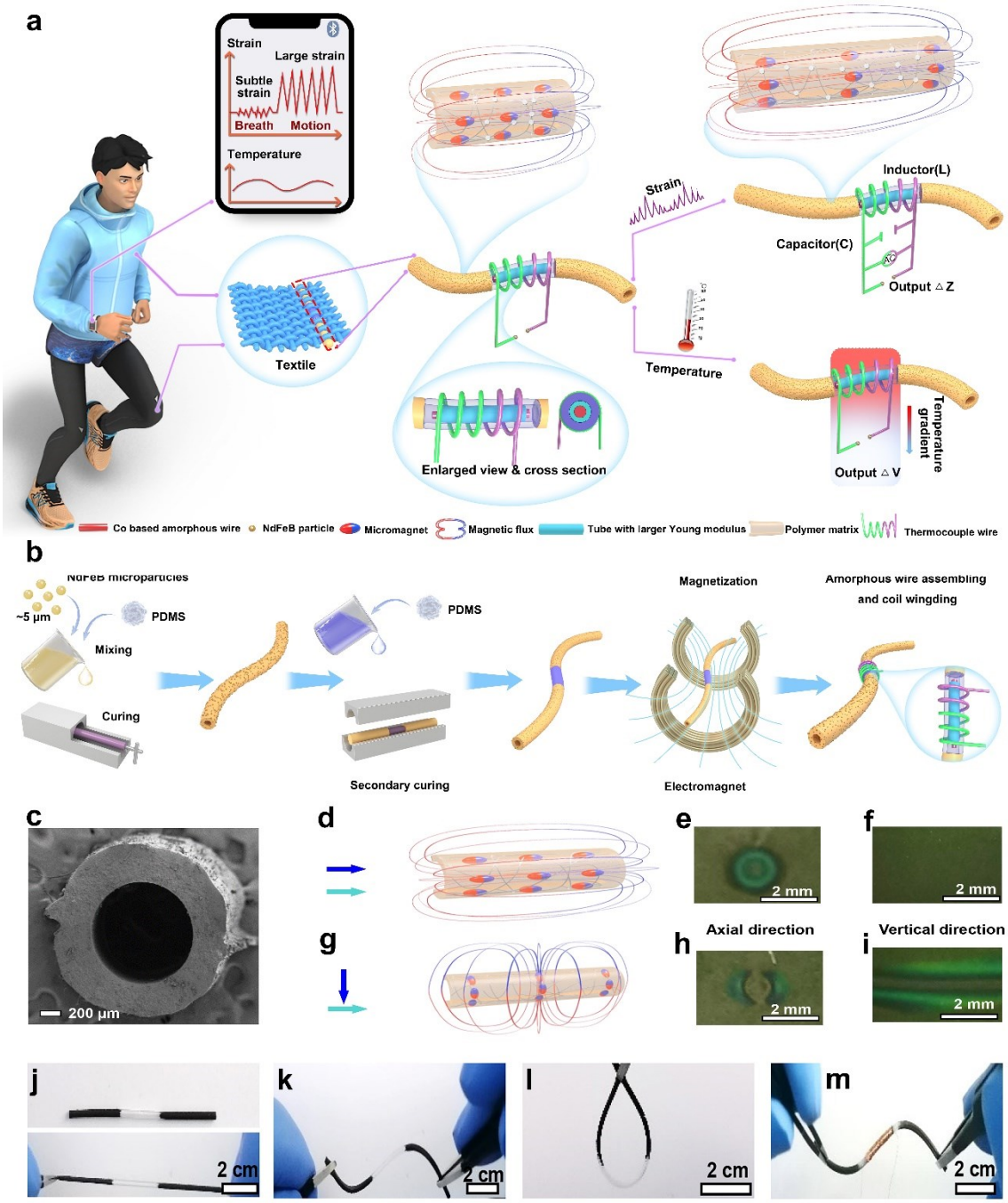

Figure 1. Characterization and fabrication process of STDMS. **(a)** Schematics revealing a possibility to use STDMS for cross-talk free assessment of strain and temperature information for the specific example of smart wearables. **(b)** Schematics of the fabrication process of STDMS. **(c)** A cross-section SEM image of a tube-shaped magnetic composite. **(d, g)** Schematic diagram of the magnetization direction within the composite and magnetic induction lines of the magnetic composite. Blue and cyan arrows indicate the

direction of the magnetized impulse fields and the axial of magnetic composite tube, respectively. Imaging of magnetic induction lines taken with an indicator film in the **(e)** axial and **(f)** radial directions taken of a tube-shaped magnetic composite magnetized in the axial direction (compare to the schematics in panel **(d)**). Imaging of magnetic induction lines taken with an indicator film in the **(h)** axial and **(i)** radial directions taken of a tube-shaped magnetic composite magnetized in the radial direction (compare to the schematics in panel **(g)**). **(j-l)** Optical micrographs showing the sensor without CNC thermocouple and without integrated CoAW. Two darker regions at each side of the sensor tube are tube-shaped magnetic composites. The transparent part in the middle is PDMS. The sensor can be stretched, bent, or twisted. **(m)** Optical micrograph showing the assembled STDMS sensor with inserted CoAW and wound CNC thermocouple in the central region of the sensor structure. The STDMS maintain the mechanical flexibility.

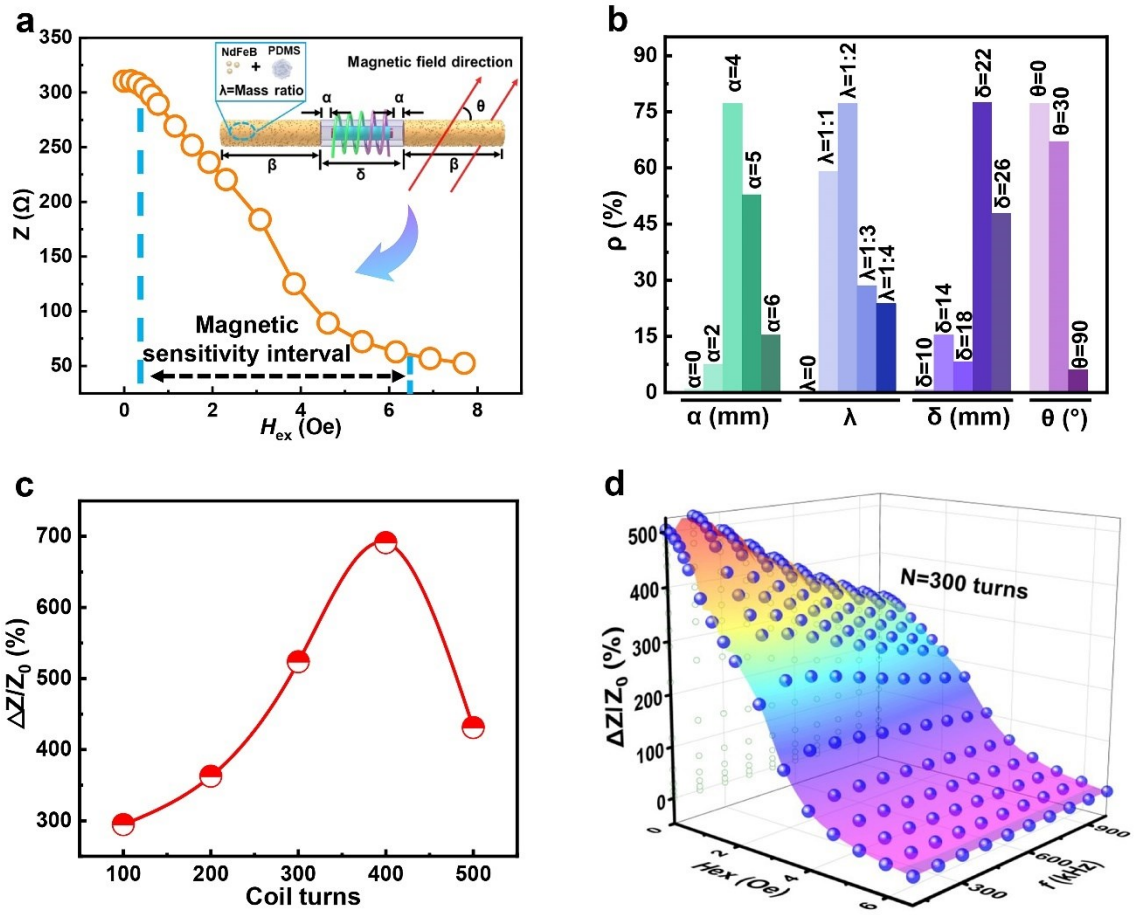

Figure 2. Tailoring the strain sensing performance of STDMS architectures. **(a)** The change of the electrical impedance of the only CoAW in an applied external magnetic field taken at optimal number of coil turns (N = 300) and optimal measurement frequency (f = 500 kHz). Insert is the schematic diagram of the STDMS with relevant geometrical parameters (α, β, δ) indicated for clarity. The content of magnetic powder in the tube-shaped magnetic composite is characterized by the parameter λ. Number of windings in the CNC thermocouple is N. The direction of the applied magnetic pulsed field is characterized by the angle θ. The purpose of regulating all parameters is to make the magnetic field provided by the magnetic composite match the magnetic sensitivity interval corresponding to the maximum impedance variation of the CoAW. **(b)** The sensitivity factor ρ as function of relevant parameters characterizing the STDMS architecture: α, λ, δ, θ. **(c)** Maximum relative change of the impedance ($\Delta Z/Z_0$) of the

CoAW containing CNC coils with a different number of turns, here, the relative change of the impedance is caused by applied external magnetic field. **(d)** Relative change of the impedance ($\Delta Z/Z_0$) with applied external magnetic field of the CoAW containing CNC coils with N = 300. The impedance is measured at different frequency and external magnetic field.

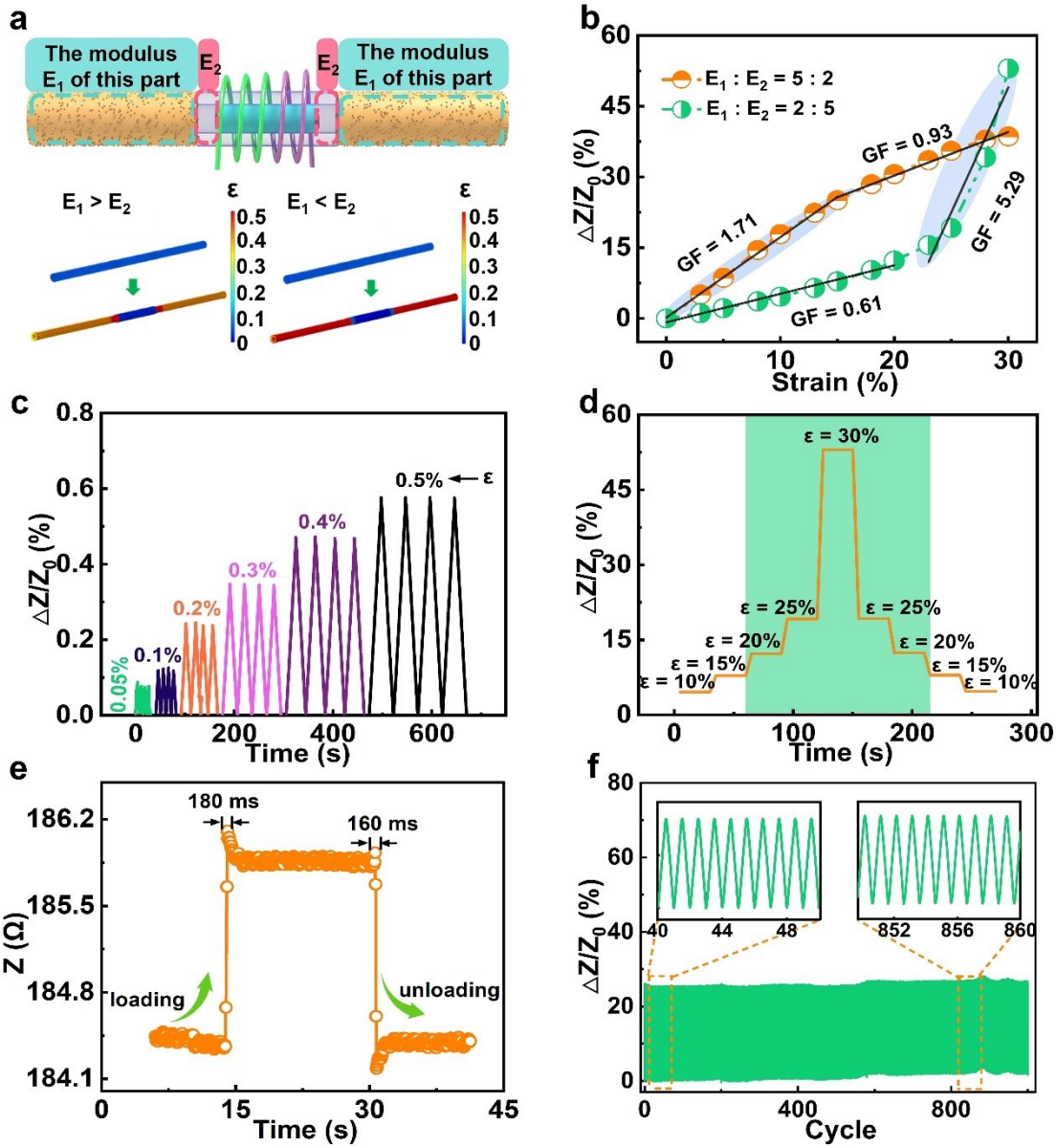

Figure 3. Strain sensing performance of the STDMS. **(a)** Mechanocombinatoric screening of the strain sensitivity of the STDMS architecture based on strain

redistribution within the heterogeneous structure ($\alpha = 4$ mm, β=22 mm, λ=1:2, θ=0°). The Young's modulus of the tube-shaped magnetic composite is E_1 (region of length β indicated in **Figure 2**a). The Young's modulus of the nonmagnetic PDMS cylinder is E_2 (region of length α indicated in **Figure 2**a). **(b)** Relative impedance changes as function of applied strain for STDMS with $E_1 : E_2 = 2 : 5$ (light green symbols) and $E_1 : E_2 = 5 : 2$ (orange symbols). The slope of the linear fit provides access to the gauge factor (GF). **(c)** Relative impedance change of the STDMS-E_1 architecture (E_1 = 0.576 MPa; E_2 = 0.239 MPa) under cyclic tensile loading with different amplitude of the applied strain ε (the case of small strain). **(d)** Relative impedance change of the STDMS-E_2 architecture (E_1 = 0.166 MPa; E_2 = 0.392 MPa) during stretching and releasing process (the case of larger strain). **(e)** Measurement of the response time of the STDMS-E_1 architecture at a fast loading and unloading cycle. **(f)** Relative impedance change of the STDMS-E_1 architecture over 1000 stretching and releasing cycles at strain from 0 to 15%.

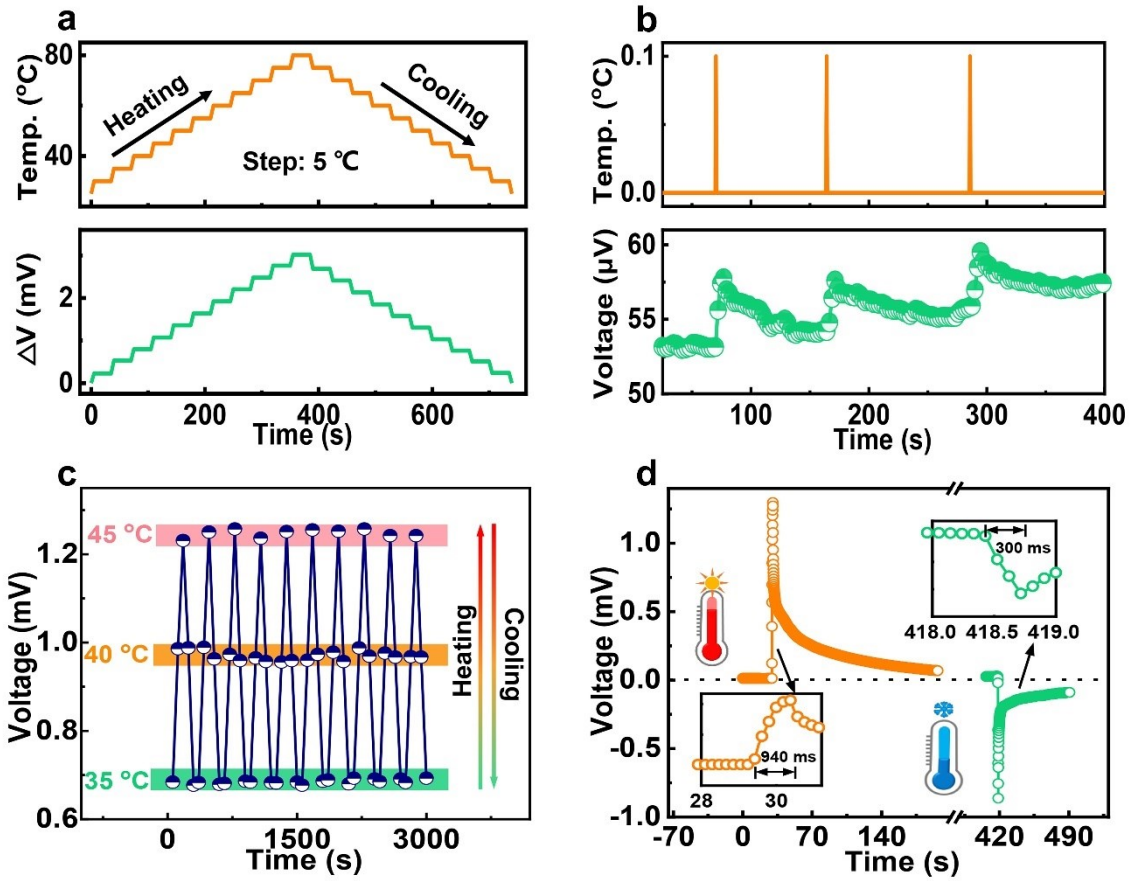

Figure 4. Temperature sensing performance of the STDMS. **(a)** Output voltage measured by the CNC thermocouple coiled around the sensing architecture during the heating and cooling process (gradient temperature was changed from 0°C to 55 °C and back to 0 °C). **(b)** The output voltage of the STDMS with a temperature gradient of 0.1 °C. **(c)** Output voltage of the CNC thermocouple over 10 heating and cooling cycles between 35 °C and 45 °C. The voltage output at 40 °C was also tested as it is closer to the actual temperature of the human body. **(d)** Measurement of the response time of the CNC thermocouple approached with a heating (cooling) source of 50 (10) °C. All the temperature performance measurement were select STDMS-E_1 and $\alpha = 4$ mm, β=22 mm, λ=1:2, θ=0°, respectively.

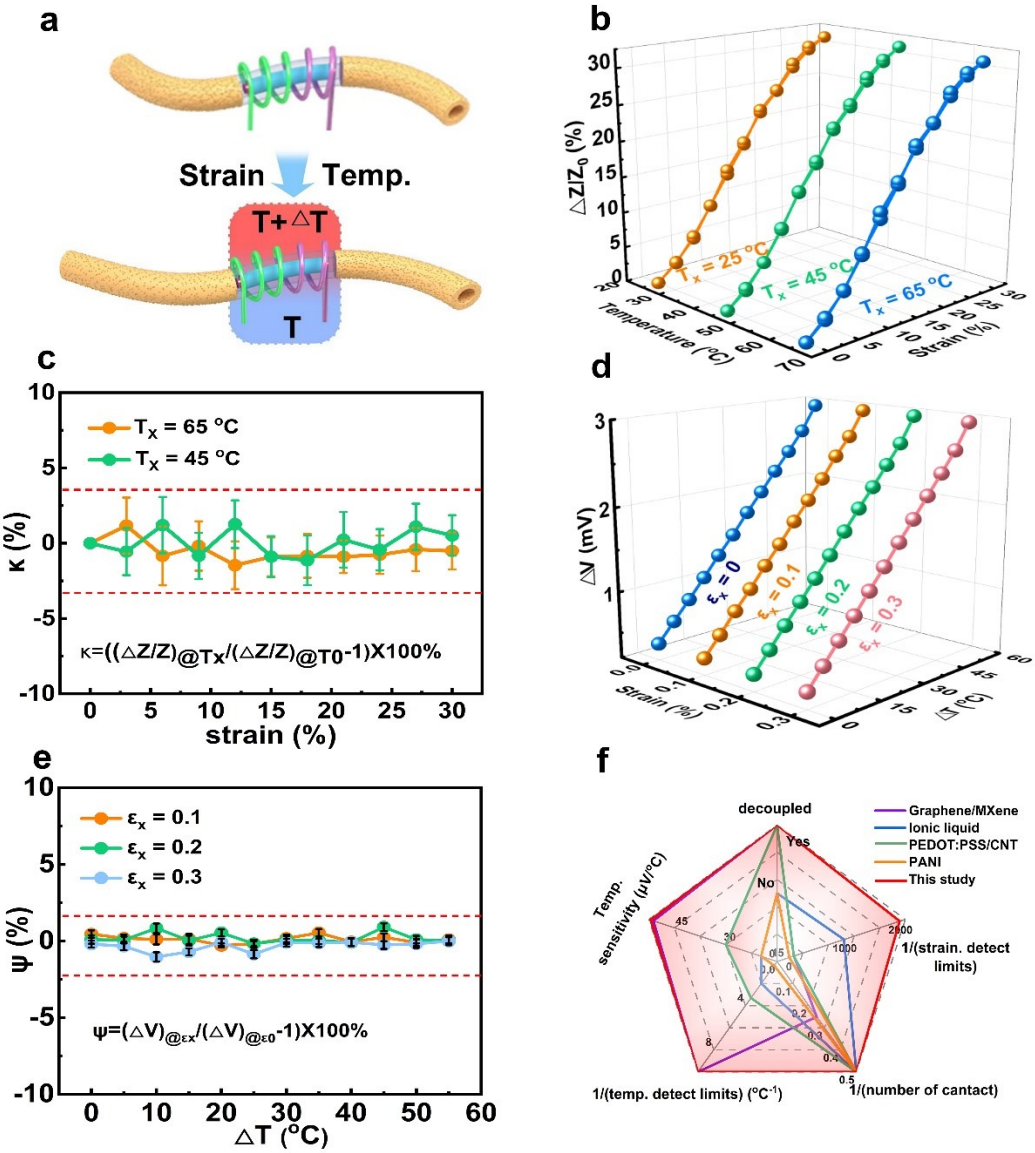

Figure 5. Characterization of the STDMS devices upon thermal and mechanical stimuli. **(a)** Schematic diagram of the effect of strain and temperature on the detection performance of the STDMS. **(b)** Relative change of impedance of the STDMS architecture taken upon applying tensile strain to the device at different temperature. **(c)** The variation factor κ as function of the applied strain under different temperature. **(d)** The change of the output voltage of the CNC thermocouple with temperature measured at constant strain (relaxed state). **(e)** The variation factor ψ as function of the temperature with different strain. **(f)** Performance comparison of the STDMS with other dual mode

sensors. Here, the parameter of STDMS was selected as optimal value (i.e., α = 4 mm, β=22 mm, λ=1:2, θ=0°), measurement of (**b**-**e**) were performed on the STDMS- E_1.

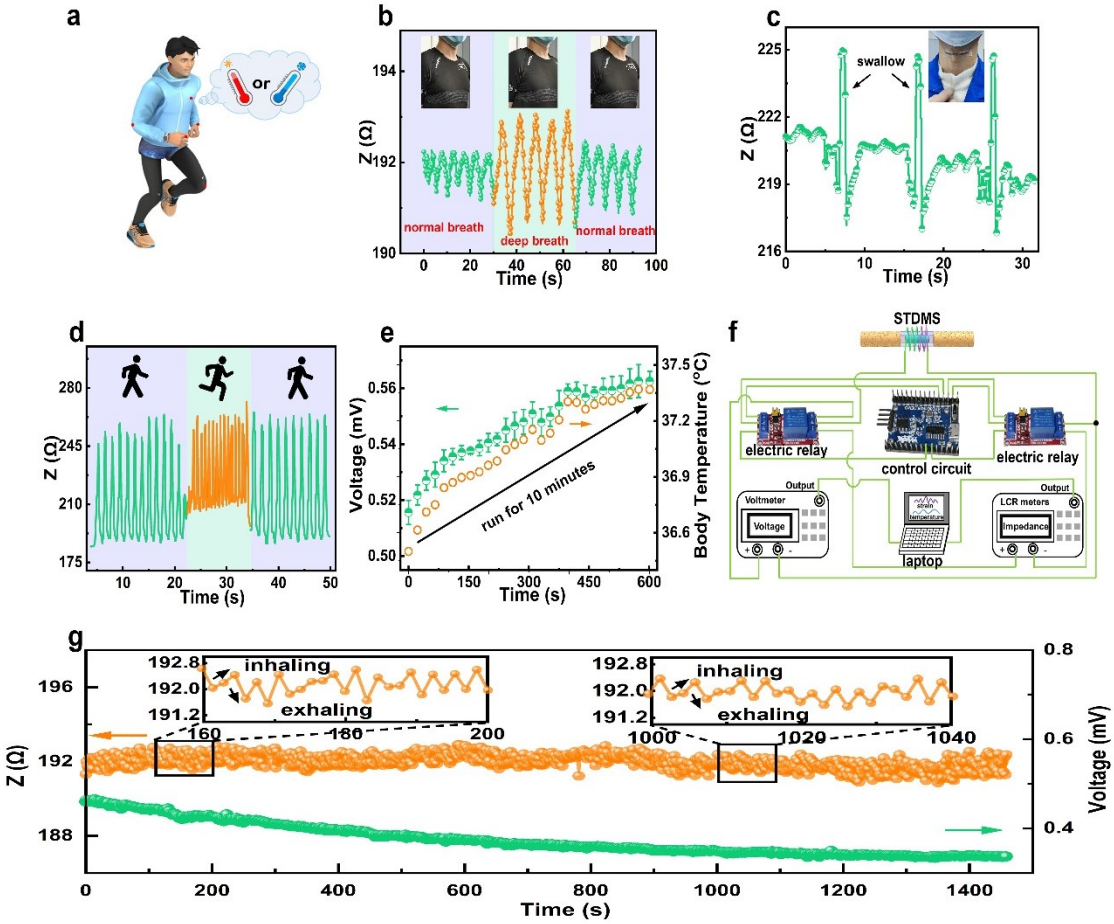

Figure 6. In situ human physiology and environmental temperature monitoring using the STDMS. **(a)** Schematics indicating that STDMS can be applied at different location of the human body, say integrated within cloth, for strain and temperature detection. **(b)** Impedance response of the STDMS mounted on the chest for breath monitoring. **(c)** Impedance response of the STDMS for swallow detection. **(d)** The impedance changes of the STDMS in response to knee bending. **(e)** voltage response of the STDMS mounted on the chest for temperature monitoring during running. **(f)** Control circuit for detecting temperature and strain of the STDMS. **(g)** Real-time output impedance and voltage of the

STDMS (mounted on a breathing belt) corresponding to the breath and environment temperature under a variation temperature of surroundings from 25 °C to 29 °C.

Table 1. Comparison table of strain-temperature dual mode sensors.

Sensing materials	**Decouple**	**Strain detect limit**	**Strain-GF**	**Temp. detect limit (℃)**	**Temp. sensitivity ($℃^{-1}$)**	**Ref.**
XSBR/SSCNT	**N**	**0.01**	25.98	**-**	0.01636	**[23]**
IL	**N**	**0.001**	0.824	**0.5**	0.0094	**[24]**
AgNWs	**N**	**0.002**	34.06	**-**	2600	**[26]**
CNTs/CB	**N**	**0.01**	2.1	**-**	0.00935	**[29]**
PANI	**N**	**0.05**	18.28	**2.7**	0.016	**[11]**
G/MXene	**Y**	**-**	3.7	**0.1**	53.6 μV	**[19]**
PEDOT:PSS/CNT	**Y**	**-**	-	**0.3**	31 μV	**[31]**
MAPT	**Y**	**-**	1933.3	**0.2**	25.3μV	**[30]**
BP@LEG	**Y**	**0.00023**	2765	**-**	0.00174	**[13]**
rGO	**Y**	**0.003**	-	**-**	Color reflect	**[33]**
NP/CNC/CoAWs	**Y**	**0.0005**	**5.29**	**0.1**	**54.49 μV**	**This study**

Journal's Table of Contents:

A dual-mode elastic sensor consisting of a tubular mechanically heterogeneous structure and featuring a hybrid detection mechanism enables real-time measurement of strain and temperature stimuli without interference. Our sensor exhibits high detection accuracy of 0.05% strain and 0.1 °C. To highlight application potential, we integrated the sensor in textile to detect breathing/human-movement and body temperature continuously and independently, as well as ambient temperature.

Keyword: Dual-mode sensors, Magnetoelastic effect, Co-based amorphous wire, Thermoelectricity, Smart wearables

Huiyun Xiao, Shengbin Li, Zidong He, Yuanzhao Wu, Zhiyi Gao, Chao Hu, Siqi Hu, Shengding Wang, Chao Liu, Jie Shang, Meiyong Liao, Denys Makarov*, Yiwei Liu*, Run-Wei Li*

Title: Dual mode strain-temperature sensor with high stimuli discriminability and resolution for smart wearables

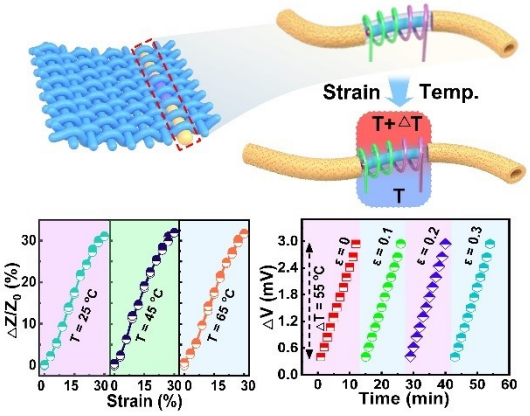

WILEY-VCH

ADVANCED FUNCTIONAL MATERIALS

Supporting Information

for Adv. Funct. Mater., DOI:

Dual mode strain-temperature sensor with high stimuli discriminability and resolution for smart wearables

Huiyun Xiao, Shengbin Li, Zidong He, Yuanzhao Wu, Zhiyi Gao*, Chao Hu, Siqi Hu, Shengding Wang, Chao Liu, Jie Shang*, *Meiyong Liao*, Denys Makarov*, *Yiwei Liu**, *Run-Wei Li**

Supplementary Information

Dual mode strain-temperature sensor with high stimuli discriminability and resolution for smart wearables

Huiyun Xiao[a,b,c], *Shengbin Li*[a,b,c], *Zidong He*[a,b,c], *Yuanzhao Wu*[a,b,c], Zhiyi Gao[a,b,c], *Chao Hu*[b], *Siqi Hu*[b], *Shengding Wang*[a,b,c], *Chao Liu*[b,d], *Jie Shang*[a,b,c], *Meiyong Liao*[a,e], Denys Makarov[f,*], *Yiwei Liu*[a,b,c,*], *Run-Wei Li*[a,b,c,*]

[a]CAS Key Laboratory of Magnetic Materials and Devices,
Ningbo Institute of Materials Technology and Engineering, Chinese Academy of Sciences, Ningbo 315201, P. R. China

[b]Zhejiang Province Key Laboratory of Magnetic Materials and Application Technology,
Ningbo Institute of Materials Technology and Engineering, Chinese Academy of Sciences, Ningbo 315201, P. R. China

[c]University of Chinese Academy of Sciences, Beijing 100049, P. R. China

[d]School of Material Chemistry, Ningbo University, Ningbo, Zhejiang 315201, P. R. China

[e]National Institute for Materials Science, 1-1 Namiki, Tsukuba, Ibaraki 305-0044, Japan

[f]Helmholtz-Zentrum Dresden-Rossendorf e.V., Institute of Ion Beam Physics and Materials Research, Bautzner Landstrasse 400, 01328 Dresden, Germany

Corresponding author: Yiwei Liu, Denys Makarov, Run-Wei Li

E-mail: liuyw@nimte.ac.cn (Prof. Y. W. Liu); d.makarov@hzdr.de (Dr. D. Makarov); runweili@nimte.ac.cn (Prof. R.-W. Li)

Telephone: +86-574-87617212

Fax: +86-574-87617212

This file contains:

Figure S1-S30

Characterization of the structural, magnetic properties, and mechanical properties of tube-shaped magnetic composite, simulation data of the magnetic field provided by the magnetic composite, structure and magnetic properties of CoAWs, $\Delta Z/Z_0$ of STDMS variation with different parameters (α, β, δ, θ, λ, N, f), structure and thermoelectric properties of CNC thermocouple, Summary of the strain and temperature detection limitation, STDMS integrated in textile to detect human-movement and body temperature etc.

Video S1

Respiratory monitoring with STDMS

Video S2

Swallow monitoring with STDMS

Video S3

Ambient temperature and respiratory monitoring with STDMS

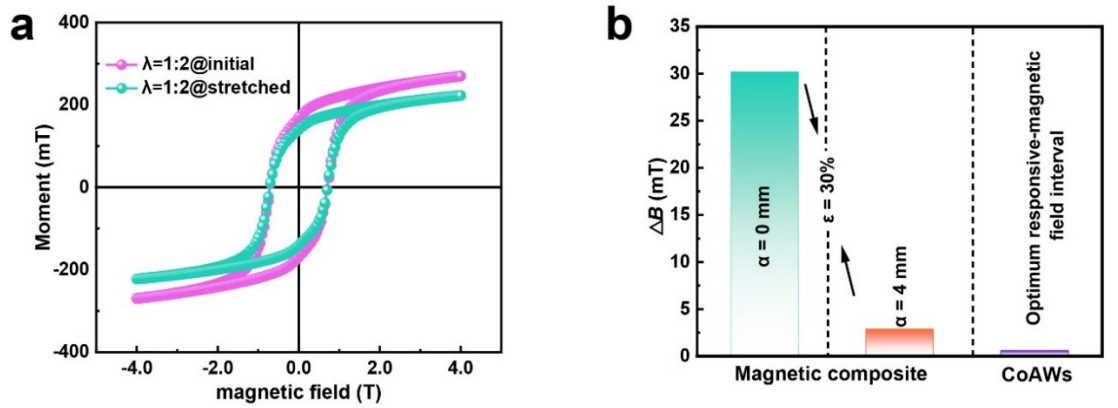

Figure S1. (a) Comparison of the magnetic moment of the magnetic composite under stretched (30%) and unstretched state. **(b)** Experimental and simulated values of magnetic field variation with strain increase to 30%, which is sufficient for CoAWs to optimally respond to the required magnetic field variations.

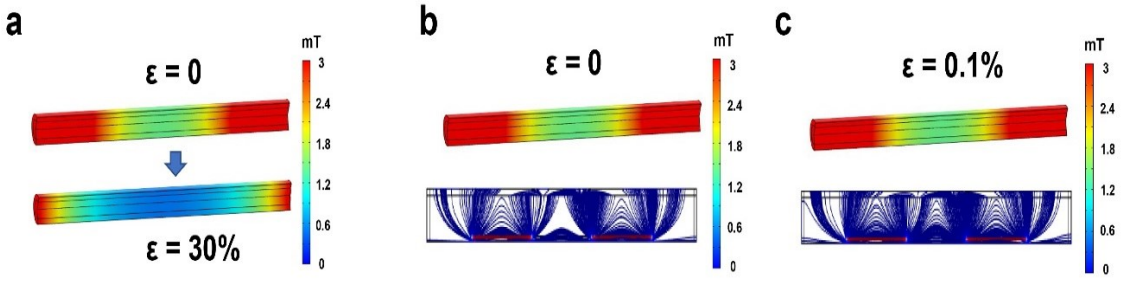

Figure S2. (a) Simulation of magnetic field variation in the middle region of the strain-to magnetic induction conversion unit as strain increases from 0 to 30%. **(b, c)** Simulation of magnetic field and induction lines variation as strain increases from 0 to 0.1%.

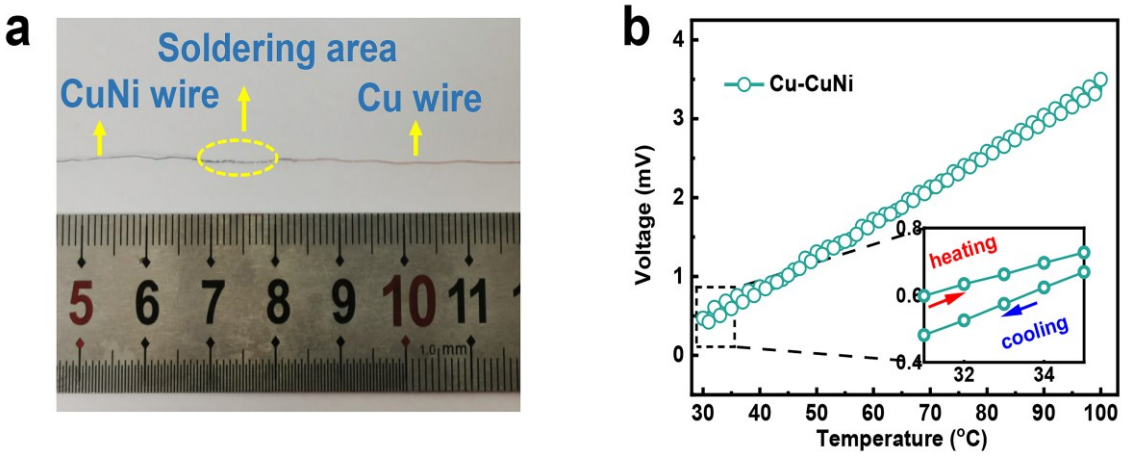

Figure S3. (a) Photograph of the CNC thermocouple. **(b)** the output voltage with the increasing temperature.

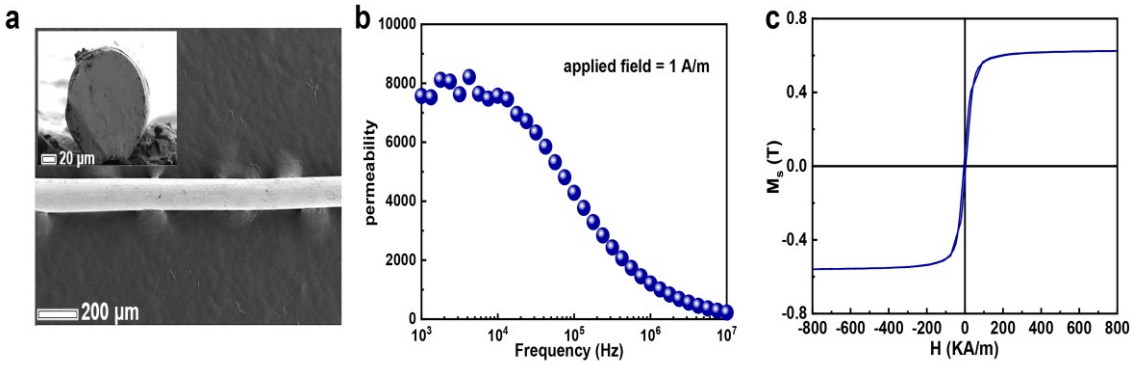

Figure S4. (a) The SEM image of CoAWs, the inset shows a cross-section of CoAWs. **(b)** permeability of CoAWs as a function of frequency under an applied field of 1 A/m. **(c)** The hysteresis loop of CoAWs.

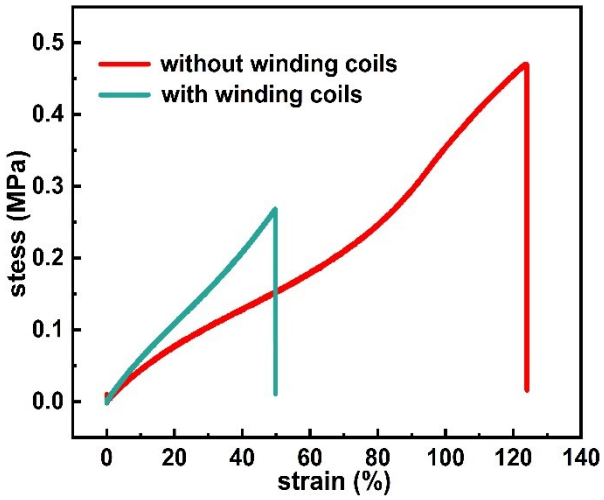

Figure S5. Tensile stress-strain curves of the strain-to-magnetic induction conversion unit with/without winding coils.

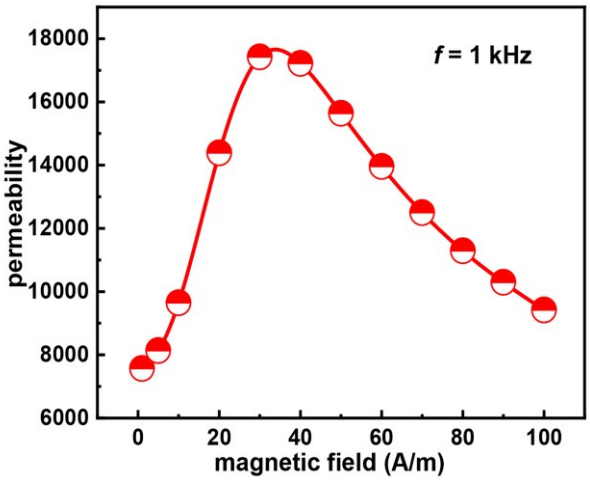

Figure S6. permeability of CoAWs as a function of magnetic field at 1 kHz.

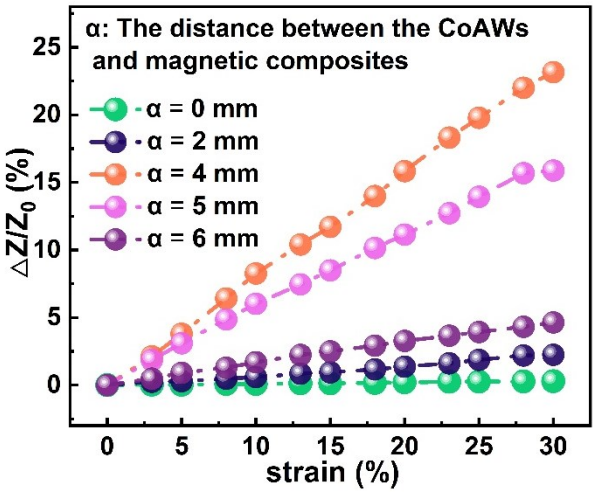

Figure S7. Plots of the η value (i.e., $\Delta Z/Z_0$) of STDMS versus strain with different α.

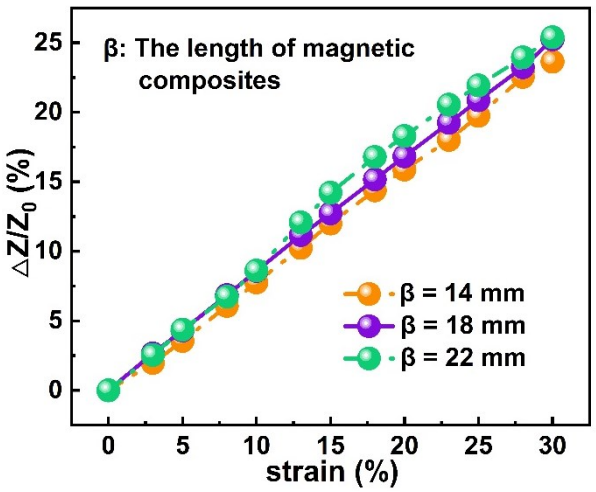

Figure S8. Plots of the η value of STDMS versus strain with different β.

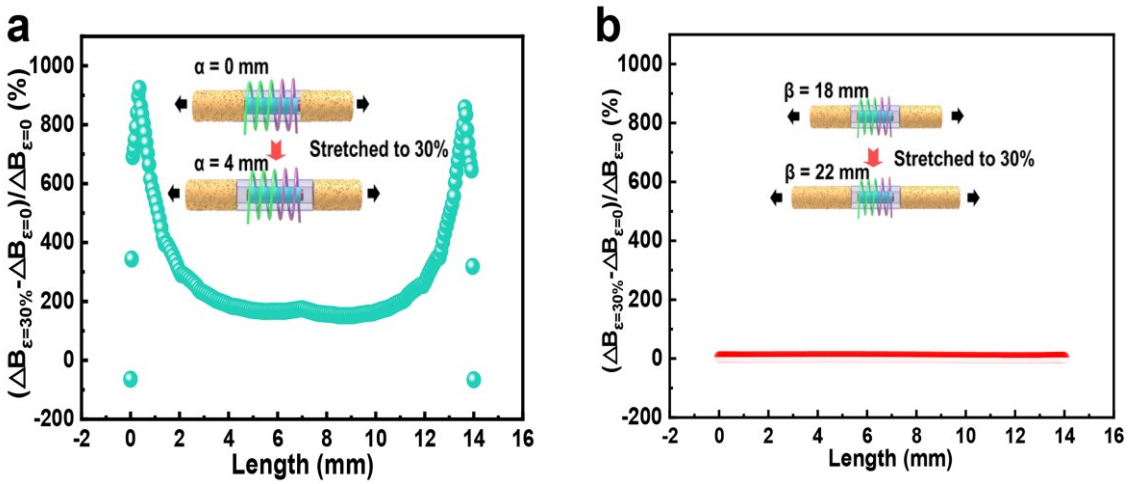

Figure S9. Simulation of the magnetic field variation with increasing strain from 0 to 30% in the CoAWs assembly region for different **(a)** α and **(b)** β.

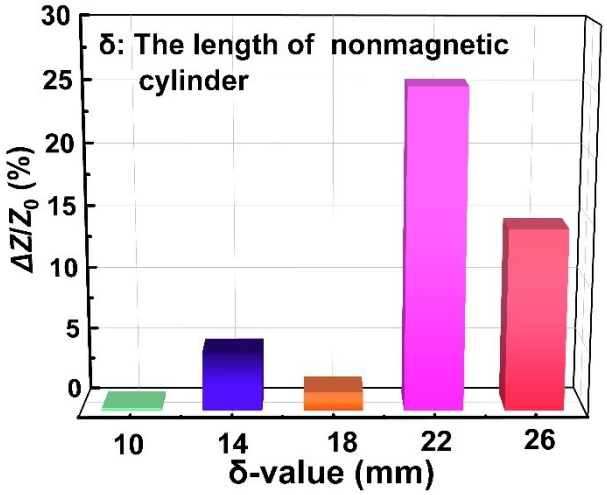

Figure S10. Plots of the η value of STDMS versus δ.

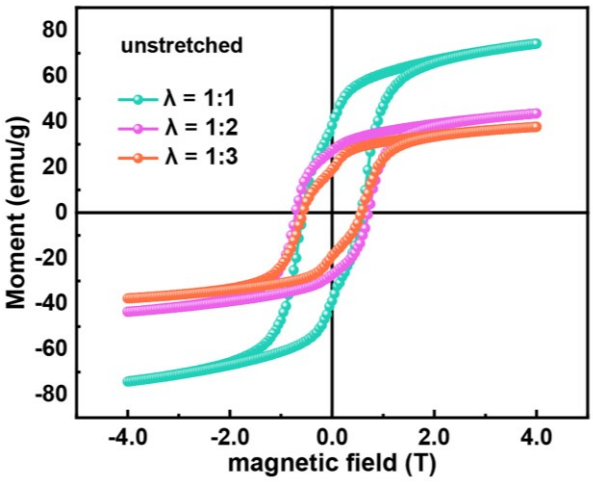

Figure S11. Comparison of the magnetic moment of the magnetic composite under unstretched state.

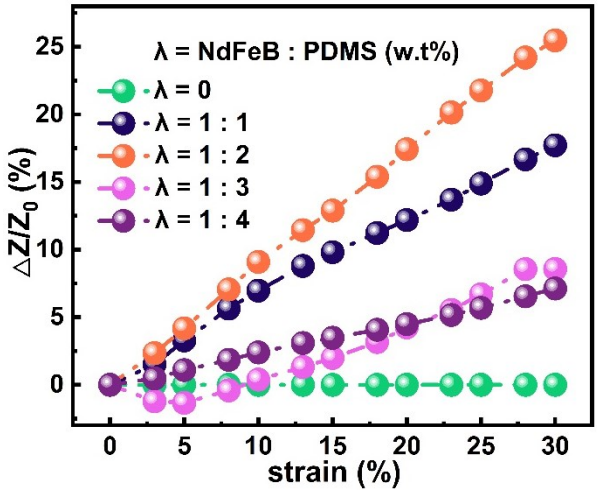

Figure S12. Plots of the η value of STDMS versus strain with different λ.

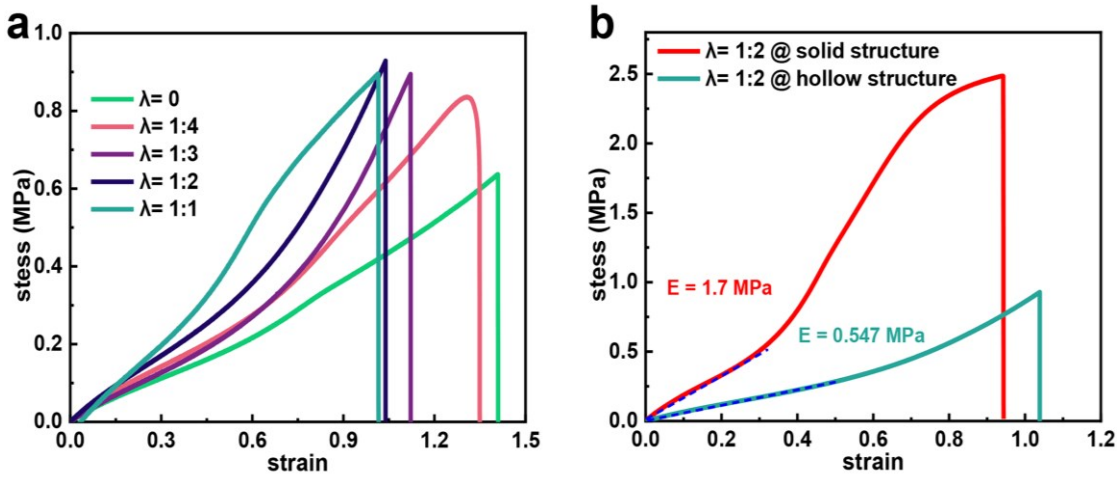

Figure S13. (a) Tensile stress-strain curves of different λ of the magnetic composite. **(b)** Tensile stress-strain curves of the tubes with hollow and solid structure.

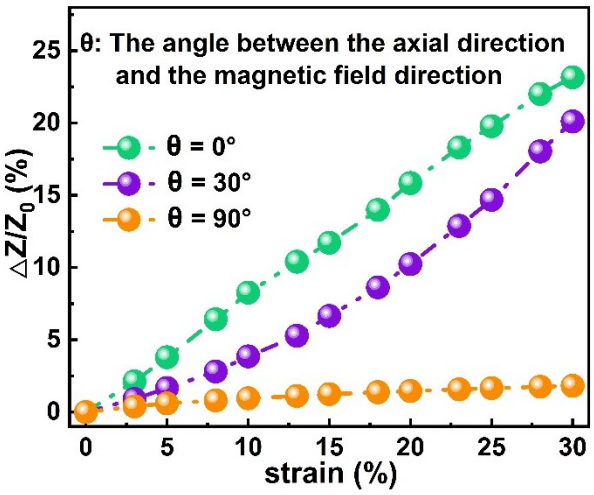

Figure S14. Plots of the η value of STDMS versus strain with different θ.

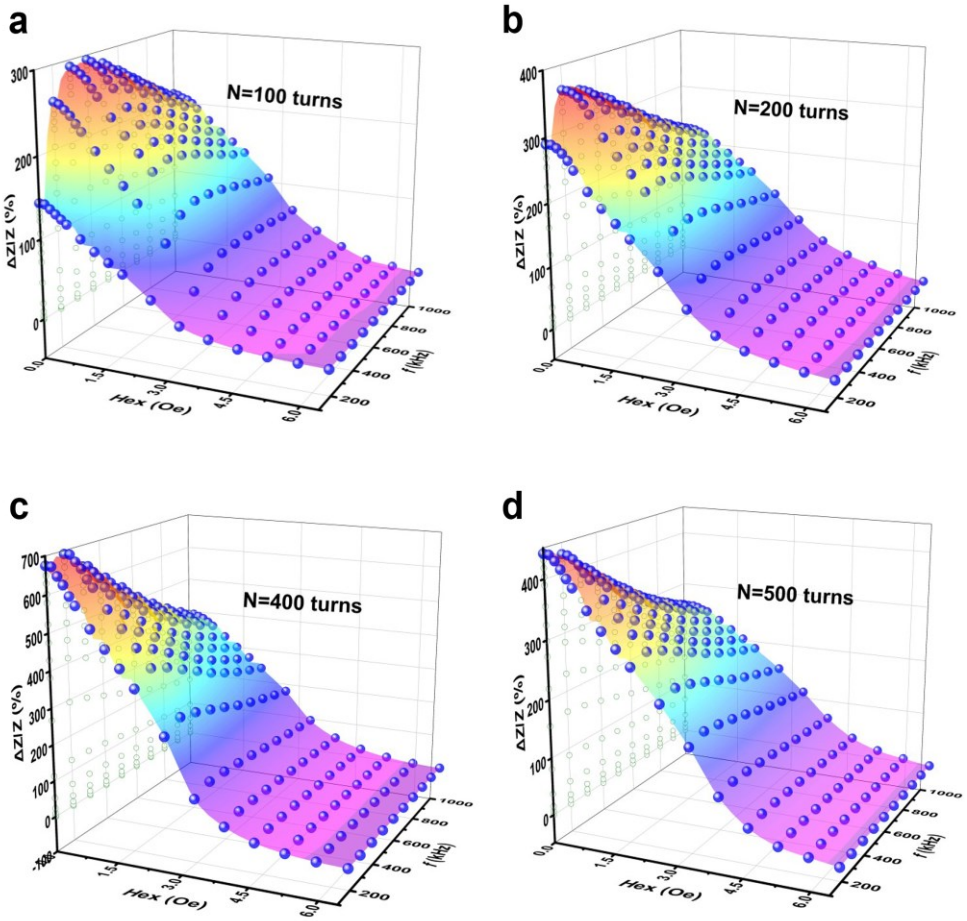

Figure S15. The $\Delta Z/Z_0$ of CoAWs with coil winding turns of 100 **(a)**,200 **(b)**, 400 **(c)**,500 **(d)** along with the applied magnetic field and excitation frequency.

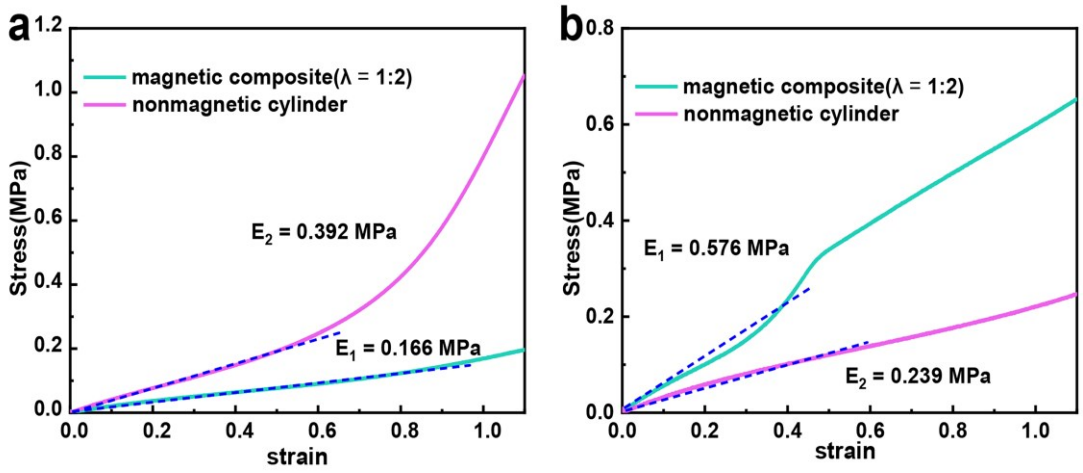

Figure S16. (a) Tensile stress-strain curves of the magnetic composite (λ=1:2, part A and part B of the PDMS with the ratio of 20:1) and the nonmagnetic cylinder (part A and part B of the PDMS with the ratio of 10:1). **(b)** Tensile stress-strain curves of the magnetic composite (λ=1:2, part A and part B of the PDMS with the ratio of 14:1) and the nonmagnetic cylinder (part A and part B of the PDMS with the ratio of 18:1).

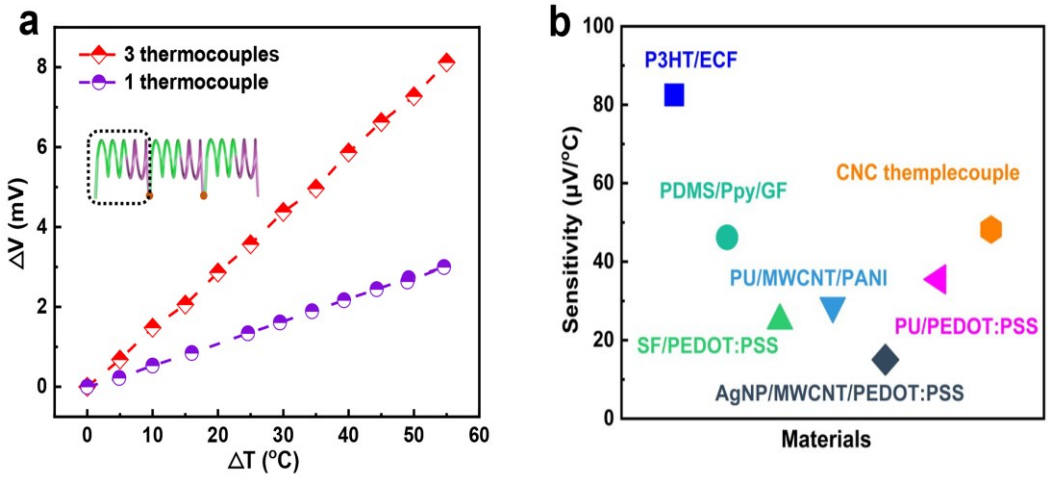

Figure S17. (a) the output voltage vs different temperature of 1 CNC thermocouple and 3 CNC thermocouples in series. **(b)** Comparison of sensitivity of different thermoelectric materials.

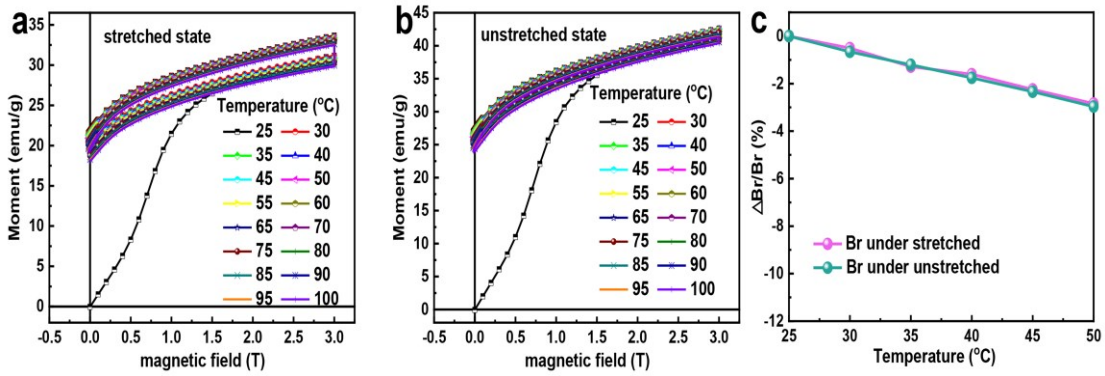

Figure S18. (a, b) Magnetic hysteresis loop of the magnetic composite at different temperature under stretched and unstretched state. **(c)** The statistics of the residual magnetism of the magnetic composite at different temperatures under stretched unstretched state, respectively.

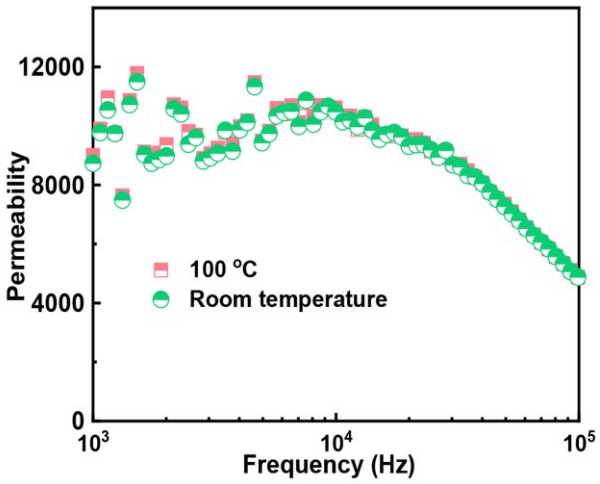

Figure S19. The permeability of FeCo-based amorphous ribbons variation with different frequency at room-temperature and 100 ℃, respectively.

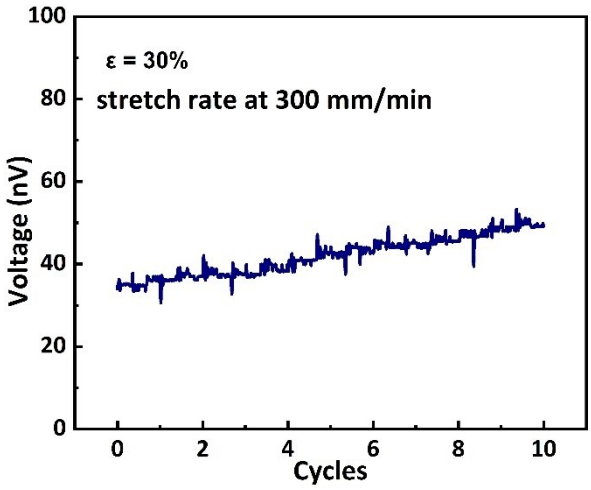

Figure S20. Output Faraday voltage of STDMS was measured for 10 cycles at a stretching rate of 300 mm/min

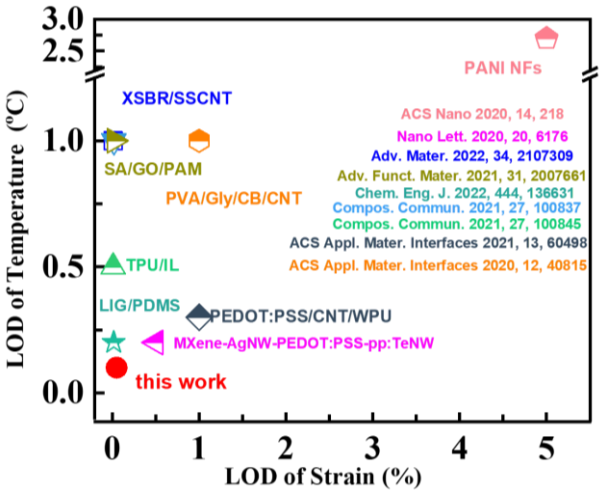

Figure S21. Summary of the strain and temperature detection limitation of the STDMS

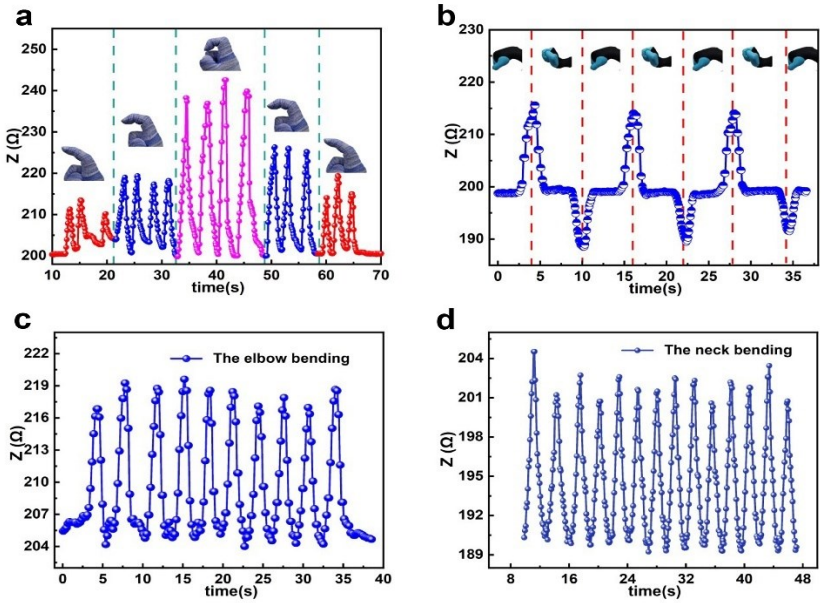

Figure S22. The impedance changes of the STDMS in response to (a) finger bending, (b) wrist bending, (c) elbow bending, (d) neck bending, (e) knee bending.

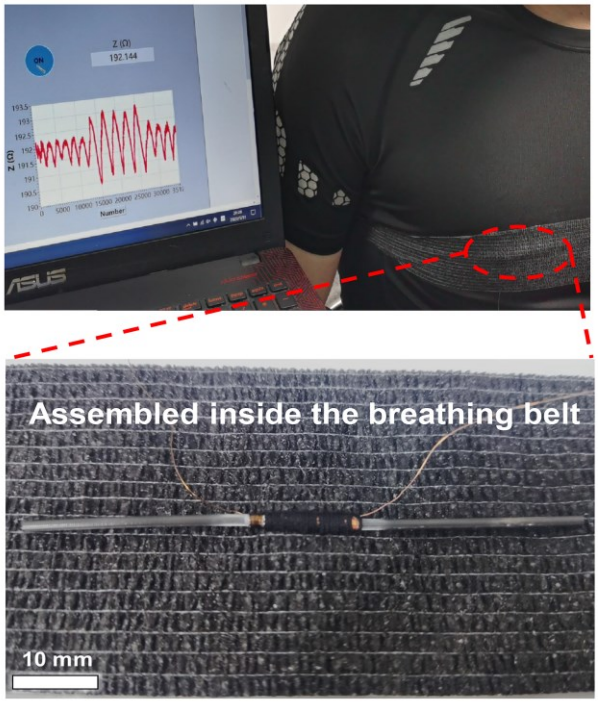

Figure S23. Photograph of the STDMS assembled in the breathing belt and an inside enlarged image.

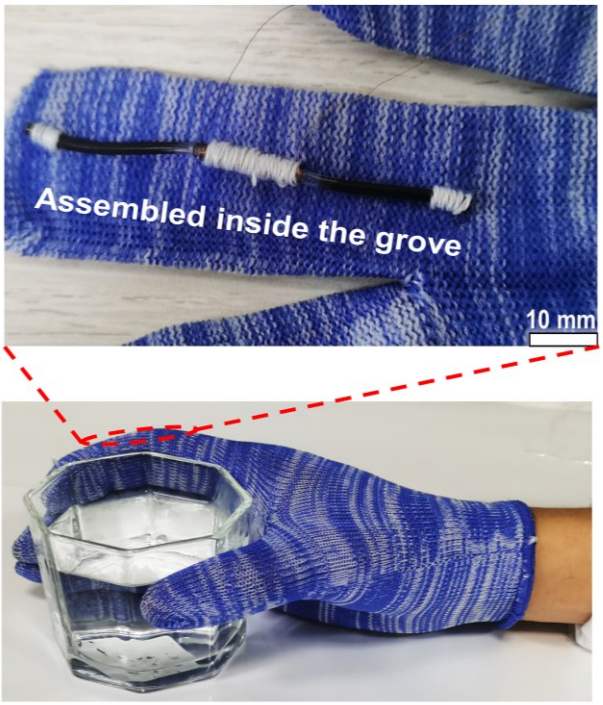

Figure S24. Photograph of the STDMS embed in the grove and an inside enlarged image.

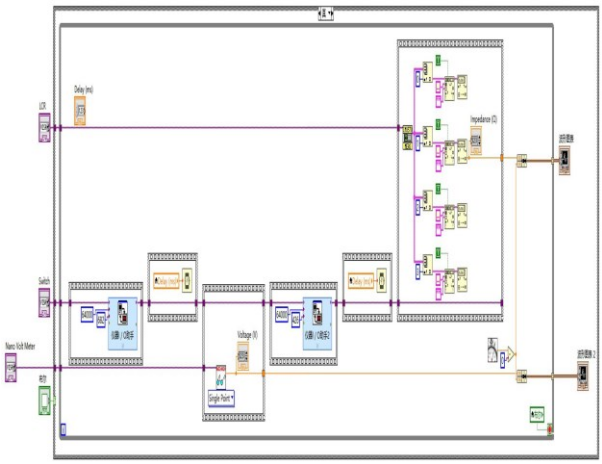

Figure S25. Output impedance and voltage reading program.

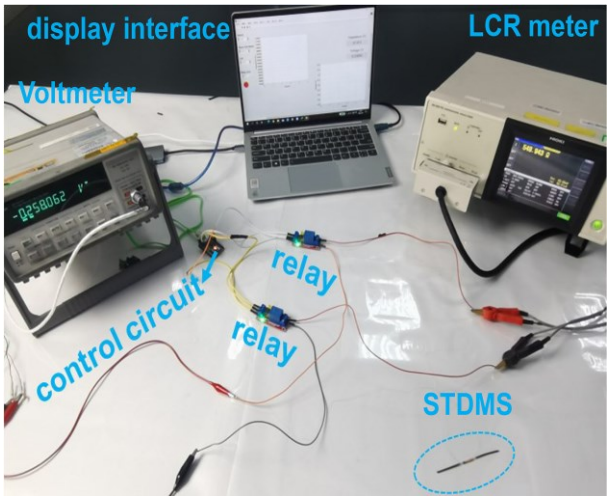

Figure S26. Photograph of the circuit for strain and temperature stimulation measurements.

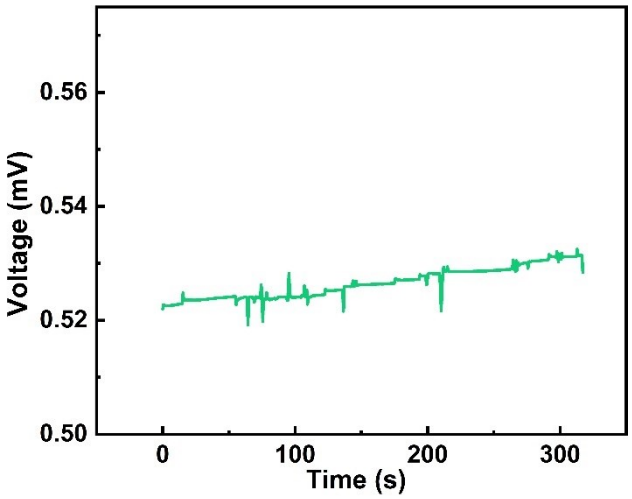

Figure S27. Variation of body temperature at relative stationary state with time.

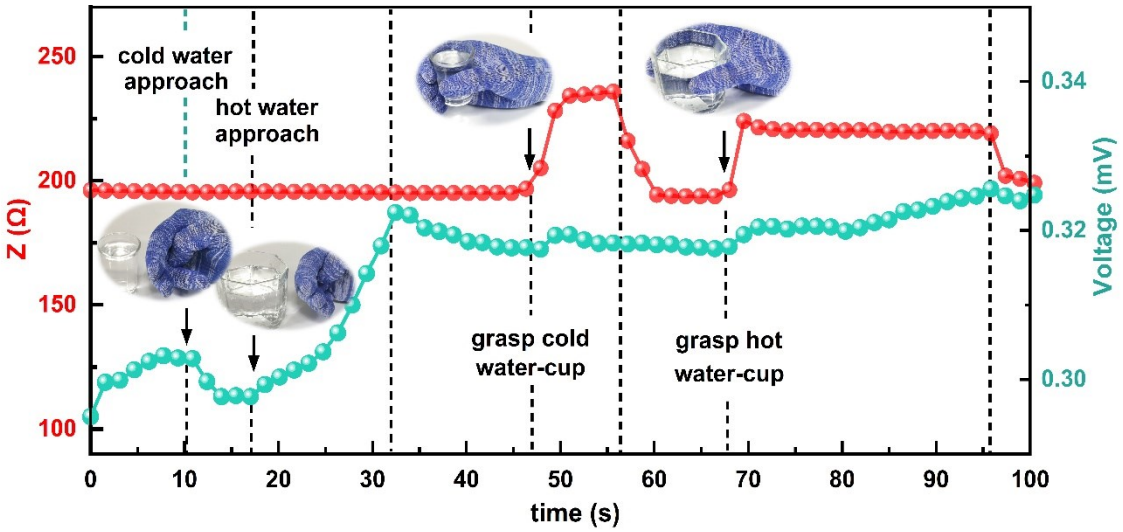

Figure S28. Real-time output impedance and voltage of STDMS (mounted on a glove) corresponding to finger strain and water temperature during the process of grasping a cup of water.

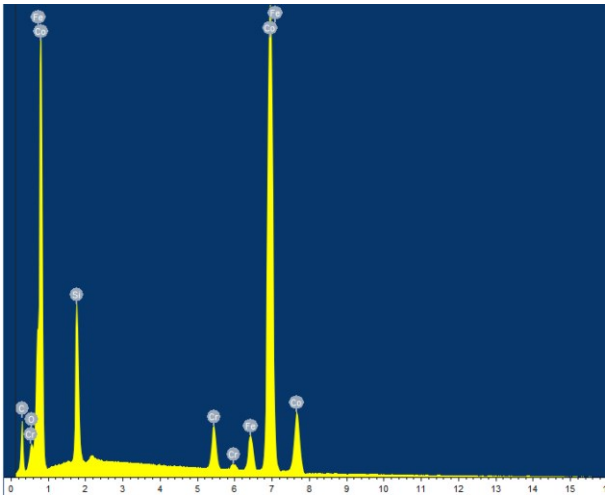

Figure S29. The EDS result of the CoAWs, showing that the alloy is composed of Co, Fe, Cr, and Si, etc.

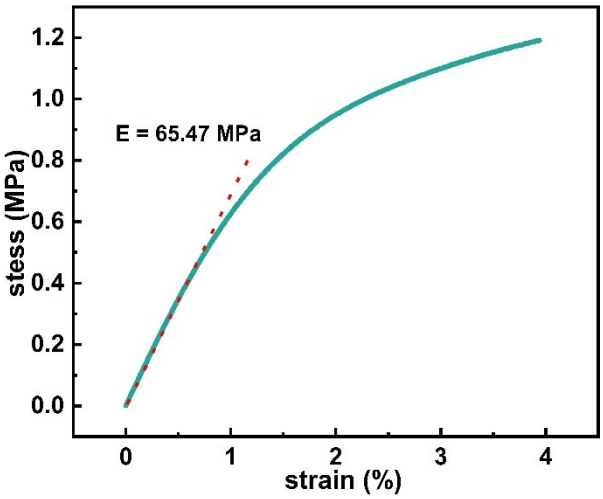

Figure S30. Tensile stress-strain curves of the PVC plastic tubes.